THESIS

INVESTIGATING SPIN WAVE DYNAMICS IN YIG MICROSTRIPS USING MICROMAGNETIC SIMULATIONS

Submitted by

Md Abu Jafar Pikul

Department of Physics

In partial fulfillment of the requirements

For the Degree of Master of Science

Colorado State University

Fort Collins, Colorado

Fall 2024

Master's Committee:

Advisor: Kristen Buchanan

Josh Berger
Carmen Menoni

Copyright by Md Abu Jafar Pikul 2024

All Rights Reserved

ABSTRACT

INVESTIGATING SPIN WAVE DYNAMICS IN YIG MICROSTRIPS USING MICROMAGNETIC SIMULATIONS

The goal of this thesis is spin wave propagation in magnetic microstrips with non-standard magnetic field directions using micromagnetic simulations. Spin waves, quasi-particles known as magnons, are waves that are generated when the electron spins oscillate collectively in a magnetic lattice. These waves can be used to transport energy. Spin waves have potential applications for microwave signal processing, logic operations, filtering, and biomedical applications. Spin waves are often launched using microstrip antennas in rectangular magnetic strips that serve as waveguides, and understanding how spin waves behave in these waveguides is critical to developing magnonics devices. The existing analytical theories that describe spin-wave behavior in microstrips are, however, limited to high-symmetry configurations (i.e., for the standard case, typically the static magnetic field direction is either parallel or perpendicular to spin waves' propagation direction) and fail to address spin-wave behavior in practical, lower-symmetry scenarios.

In this thesis, field directions of 70° and 80° are examined and compared to the surface spin wave configurations. The angle is measured with respect to the long axis (i.e., x-axis) of the microstrip antenna, and the magnetic fields are applied in the plane of the microstrip. The lower-symmetry scenarios show complex, titled diamond patterns because anisotropic dispersion relations in magnetic thin films govern spin-wave propagation. In this study, micromagnetic simulations were used to model spin wave dynamics in a series of rectangular Yttrium Iron Garnet (YIG) microstrips in low-symmetry configurations. YIG is an ideal material for spin wave investigations because it has exceptionally low damping. The spin wave behavior was analyzed in a series of simulations in which the static magnetic field direction, driving frequency, excitation type (stripline antenna or point source), and microstrip dimensions (i.e., ranges of widths 1.28 μm to 2252.8 μm)

were systematically altered. For stripline antennas, diamond-shaped spin wave propagation patterns are observed when the field is applied in-plane at 90° with respect to the long axis of the magnetic thin film, and this diamond pattern can be understood by considering the interference of width-quantized modes. As the static magnetic field direction is reduced, the diamond pattern tilts, and the outline angles are similar to what is seen for point source excitations. The micromagnetic investigations explain the discrepancy and fill the gap between the experimental observations and analytical calculations. These findings enhance our understanding of spin wave dynamics and will be useful for the development of advanced magnonics devices and information processing technologies.

ACKNOWLEDGEMENTS

I am truly grateful to Professor Kristen Buchanan for her exceptional guidance and support throughout my research. Her insightful feedback and expertise have played a crucial role in shaping my knowledge of magnetism and this thesis. I deeply appreciate her unwavering mentorship.

I would also like to thank my group members, Mitchell Swyt, Lia Compton, Byron Fritch, and David Marchfield, as well as Emeritus Professor Carl Patton. Their engaging conversations and support have been invaluable to me. I am so greatly thankful to Mitchell and Lia for introducing the labs. Finally, I am thankful to my family and friends for their unconditional love.

I acknowledge support from the W. M. Keck Foundation and NSF EFMA-1741666.

TABLE OF CONTENTS

LIST OF TABLES

LIST OF FIGURES

Chapter 1

Introduction

1.1 Motivation

The propagation of spin waves in magnetic materials has gained significant attention due to their potential applications in spintronics [2] and magnonics [3,4]. Spin waves, known as magnons, are collective excitations of the electron spins in a magnetic material that can be used to transmit information and perform logical operations [5–8]. Yttrium Iron Garnet (YIG) is an attractive material for studying spin wave dynamics because its damping parameter is low [6], which allows for the efficient propagation of spin waves over long distances, which is crucial for developing practical magnonic devices. Previous studies have demonstrated the potential of YIG for various applications, including magnonic crystals and spin wave logic gates [9, 10]. However, many of these studies have been limited to high-symmetry configurations, which do not fully exploit the rich potential of spin waves for applications [11].

Micromagnetic simulations [12, 13] have emerged as a powerful tool for investigating spin wave phenomena in complex geometries and under varying field configurations [11]. These simulations enable the calculation of spin wave dispersion relations, which describe the relationship between wave frequency and wave vector that are critical for understanding how spin waves propagate and interact in a magnetic material [14]. Using micromagnetic simulations, it is possible to explore lower-symmetry directions and more intricate geometries that are challenging to analyze using analytical methods [15]. The motivation for this thesis is to enhance the understanding of spin wave dynamics in YIG microstrip with non-standard magnetic field configurations through detailed micromagnetic simulations. This research investigates the effects of various factors, including static magnetic field directions, driving frequency, type of excitation (stripline antenna or point source), position of the point source, and dimensions of the microstrip. This work aims to advance fundamental knowledge of how spin waves propagate in lower symmetry field con-

figurations and pave the way for developing advanced magnonic devices that could revolutionize information processing technologies.

This research is motivated by the complex spin wave behaviors that have been observed in recent experiments, particularly in Ref. [1]. Fig. 1.1 shows time-integrated Brillouin light scattering (BLS) intensity maps obtained at a frequency of 4.320 GHz with the external magnetic field applied at an angle of $\phi = 20^\circ$ with respect to the y axis (i.e., $\phi = 70^\circ$ with respect to the x axis). Figure 1.1 shows spin wave propagation patterns within a 2D magnonic crystal that involves the formation and interaction of spin wave caustic beams, which are narrow beams formed by wave propagation in preferred directions governed by spin wave dispersion relations. In Fig.1.1, the spin waves are generated by a microstrip antenna located on the left side of the images just outside of the scan region. A strong initial bright beam is observed near the bottom of the antenna, which interacts with the sample edge, creating two main initial beams. These beams are aligned with a series of wells, and scattered into additional caustic beams that appear as bright tracks radiating from the wells. Upon interaction with the YIG film edge, new caustic beams are also formed, which are seen as bright, coherent beams after the edge interactions (black and white arrows). The angles of propagation for these caustic beams are measured and found to be $\theta_{\text{vg}} = 48.38^\circ$ with respect to magnetic field direction **H**. This experimental image highlights the potential of caustic beams for applications requiring directional energy transport, adding functionality to magnonic devices.

In Ref. [1], the bright initial beam originating from the left side of the image was observed and used, but the physical mechanism of the beam creation was not explored. Normally point source excitations are required to create spin wave beams, but the beams seen in the left side of the Fig. 1.1 were generated using a microstrip antenna. Microstrip antennas are routinely used to generate spin waves in YIG, however, it is very difficult to generate spin waves that originate from a single point, hence the strong beam observed in Fig 1.1 is of interest since it might provide insight into a straightforward method to generate a directed beam of spin waves. Inspired by these experimental observations [1], in this thesis, micromagnetic simulations were used to investigate the spin wave dynamics in YIG thin-film waveguides in non-standard field geometries similar to that shown in

Fig. 1.1 to understand the physical mechanism of the beam formation. Through these simulations, the research aims to replicate and expand upon the experimental findings, and thereby to gain insight into the behavior of spin waves.

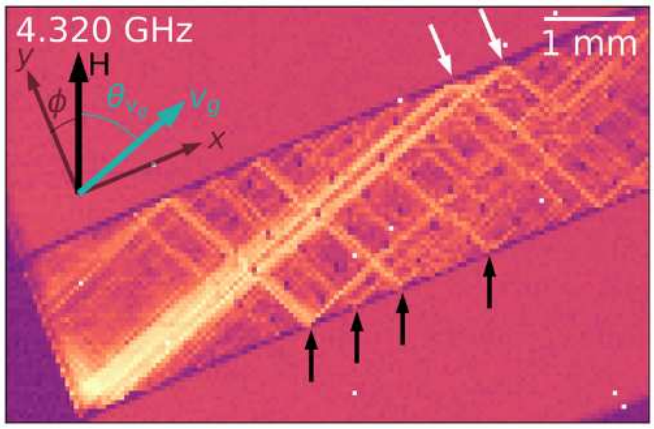

Figure 1.1: Time-integrated BLS intensity maps at 4.320 GHz with an external magnetic field applied at $\phi = 20°$ with respect to y axis (i.e., $\phi = 70°$ with respect to x axis) for a 2D magnonic crystal that consists of a periodic diamond shape array of sub-wavelength patterned wells (darker spots on the image). The initial bright beam near the bottom of the antenna interacts with the sample edge, creating main caustic beams (white arrows) and secondary caustics (black arrows) radiating from the wells. These caustic beams demonstrate highly directional energy transport within the 2D magnonic crystal [1].

1.2 Problem Statement

The development of advanced magnonic devices relies heavily on the precise control, manipulation, and understanding of how spin wave dynamics work in a magnetic material. The majority of spin wave studies are done in a configuration where the magnetic field is applied parallel or perpendicular to the spin wave propagation direction, and existing analytical theories are limited to high-symmetry configurations [16]. There are very few works that address the complexities of spin wave behavior in lower-symmetry scenarios [1, 11]. Fig. 1.1 shows that two initial beams that resemble caustics can be created using a conventional microstrip antenna (white arrows), and my goal is to explain how these initial beams form by using micromagnetic simulations because there are no existing theories that explain the experimental result. Therefore, it is crucial to investigate how these initial beams form and whether the initial beams are spin wave caustic beams [17–19].

More generally the study of how spin waves generate and propagate in low-symmetry configurations is essential for advancing magnonic device applications [10, 17, 20]. The simulations are conducted for Yttrium Iron Garnet (YIG) because YIG is one of the promising candidates for studying spin wave propagation in magnetic materials due to its low damping.

1.3 Spin Waves

A spin wave also a quasiparticle known as a magnon is a quantum dynamical excitation of magnetic material where the electron spins oscillate collectively. Spin waves can transmit energy and information without moving particles. The magnetic moment in a magnetic material originates from the orbital angular momentum and spin angular momentum of electrons. When the magnetic moments are perturbed from the equilibrium, they precess around the magnetic field shown in Fig. 1.2, and this precessional motion is similar to the precession of a spinning top. In a chain of electrons, each spin interacts with its nearest neighbor through dipolar and exchange interactions. When one spin in the chain is excited, it triggers a cascading effect causing each subsequent spin to precess with a phase shift. This sequence of precessing electrons forms a spin wave. Spin waves are useful for a wide variety of applications, including spin wave logic, signal processing, spin wave sensors, and transmitting information [3, 4, 21].

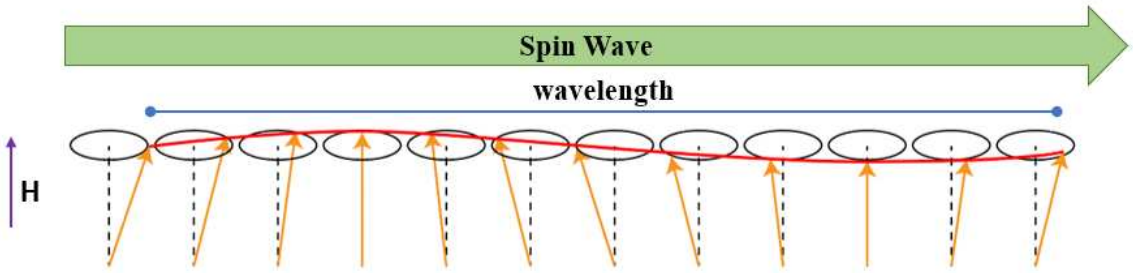

Figure 1.2: The schematic diagram of a spin wave propagating through a chain of spins in a magnetic material. The green arrow indicates the direction of the spin wave propagation, while the blue line dotted at the end denotes the wavelength. Orange arrows represent the magnetizations which precess along the direction of the external magnetic field direction **H** shown in the figure with the purple arrow. The red sinusoidal line shows the collective motion of the spins, with each moment precesses slightly out of phase with its neighbors, forming a wave pattern.

Similar to light waves and sound waves, spin waves also exhibit wave-like behaviors such as reflection and refraction [22–25], and interference [26–29]. Constructive interference occurs when two in-phase waves combine to form a wave with a higher amplitude, as shown in Fig. 1.3 (a), where the solid blue line and the dashed red line represent two in-phase waves. The superposition, shown in Fig. 1.3 (a) as a black line, results in a wave with amplified peaks and troughs. Destructive interference happens when two out-of-phase waves combine to cancel each other out. In Fig. 1.3 (b), the solid blue line and the dashed red line waves have the same frequency but are phase-shifted by π radians (180 degrees). Their superposition, shown in Fig. 1.3 (b), results in a wave with significantly reduced, in this case, zero, amplitude solid black line, illustrating the principle of wave cancellation [30].

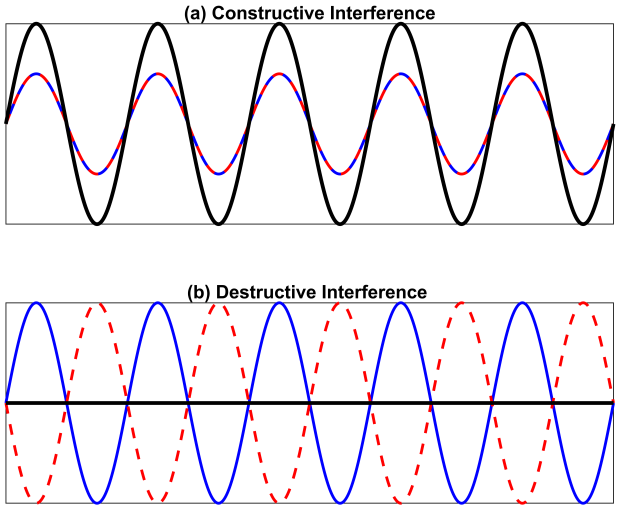

Figure 1.3: In the figure, (a) and (b) show the constructive and destructive interference patterns, respectively. In (a), the solid blue line and the dashed red line waves have the same frequency, resulting in a combined wave with a higher amplitude (black line). In (b), the solid blue line and the red dashed line waves have the same frequency but are phase-shifted by π radians, resulting in significant amplitude reduction (black line).

Some Useful Definitions

- **Spin Wave Caustics:** Spin wave caustics refer to the focusing of spin waves, which leads to a significant increase in spin wave amplitude in specific directions. Spin wave caustics

are generated in a magnetic anisotropic medium which is directional useful for transporting energy [1, 18, 19].

- **Dispersion Relation:** A dispersion relation describes how waves, such as spin waves propagate through a magnetic medium. The dispersion relation describes the relationship between the spin wave frequency and wave vector. This dispersion relation is critical for understanding how spin waves will behave. In this study, the dispersion relations are used to guide the selection of the driving frequency.

- **Magnonic Crystal:** Magnonic crystals are artificial structures designed to manipulate spin waves through periodic variations in their magnetic properties, similar to how photonic crystals control light waves. Figure 1.1 is an example of a YIG magnonic crystal.

1.4 Outline of Thesis

Spin wave propagation in Yttrium Iron Garnet (YIG) microstrips was investigated using micromagnetic simulations with the goal of understanding spin wave generation and propagation under various realistic conditions for magnonics device applications.

Chapter 1 includes the motivation and problem statement, an overview of the fundamental concepts of spin waves, their properties, behaviors, and significance in magnetic materials, along with essential definitions.

Chapter 2 details the simulation tools and methods used in the research. It describes the micromagnetic simulation software, MuMax3, the various effective magnetic fields used in the simulations, and the specific models and parameters applied to YIG microstrips.

Chapter 3 presents a comprehensive analysis of the simulation results. It covers the dynamics of magnetization under different conditions, the impact of various driven frequencies and damping factors, and the behavior of spin waves in different microstrip configurations.

Chapter 4 provides a summary and conclusions.

Chapter 2

Micromagnetic Simulations, and Model & Method

Micromagnetic simulation packages are used to understand magnetic materials such as magnetic domain formation [31], spin transfer torque [32], magnetization reversal [33], hysteresis loop [34], and domain wall dynamics [35], where the most commonly known micromagnetic packages are MuMax3 [12], OOMMF [36], and Ubermag [37].

2.1 MuMax3

MuMax3 [12] is an open-source GPU-based micromagnetic simulation tool. It is used to investigate a wide range of magnetic phenomena using the Landau-Lifshitz-Gilbert formalism. MuMax3 supports magnetostatic fields, Heisenberg exchange, RKKY coupling, Dzyaloshinskii-Moriya interaction, spin-transfer torque, uniaxial/cubic magnetocrystalline anisotropy, and thermal fluctuations. MuMax3 enables simulations involving Voronoi tessellation, time-dependent and space-dependent material parameters, and arbitrary complex excitations such as fields and currents. It can also track a moving domain wall, remove edge charges to simulate infinite geometries and apply 1D, 2D, or 3D periodic boundary conditions. Overall, MuMax3 is a powerful package that can be used to study magnetic phenomena with high computational speed and accuracy [13]. Here we use MuMax3 to investigate spin wave dynamics in a magnetic microstrip made of Yttrium Iron Garnet (YIG).

2.2 Dynamical Terms in MuMax3

2.2.1 Landau-Lifshitz-Gilbert Equation

Micromagnetic simulation packages are based on the Landau-Lifshitz-Gilbert (LLG) equation [13,37–39], which governs the time evolution of the magnetization in ferromagnetic materials [40].

The LLG equation is:

$$\frac{\partial \mathbf{m}}{\partial t} = -\frac{|\gamma|}{1+\alpha^2}\mathbf{m} \times \mathbf{H}_{\text{eff}} - \frac{\alpha|\gamma|}{1+\alpha^2}\mathbf{m} \times (\mathbf{m} \times \mathbf{H}_{\text{eff}}), \tag{2.1}$$

where, $\mathbf{m}$ represents the normalized magnetization, $|\gamma|$ is the gyromagnetic ratio, α is the dimensionless Gilbert damping constant, and $\mathbf{H}_{\text{eff}}$ denotes the effective magnetic field.

The effective magnetic field is:

$$\mathbf{H}_{\text{eff}} = -\frac{1}{\mu_0 M_{\text{s}}}\frac{\delta U}{\delta \mathbf{m}}, \tag{2.2}$$

where $\mu_0 = 4\pi \times 10^{-7}$ H/m denotes the magnetic permeability in vacuum, M_{s} is the saturation magnetization, and U is the system's energy density.

The effective magnetic is:

$$\mathbf{H}_{\text{eff}} = \mathbf{H}_{\text{exchange}} + \mathbf{H}_{\text{anisotropy}} + \mathbf{H}_{\text{dipolar}} + \mathbf{H}_{\text{Zeeman}} \tag{2.3}$$

since it include the exchange field $\mathbf{H}_{\text{exchange}}$, anisotropy field $\mathbf{H}_{\text{anisotropy}}$, dipolar field $\mathbf{H}_{\text{dipolar}}$, and Zeeman field $\mathbf{H}_{\text{Zeeman}}$. The descriptions of each are included below.

2.2.2 Exchange Field

In ferromagnetic materials, magnetic moments tend to align parallel to each other due to the exchange interaction. This interaction arises from the quantum mechanical exchange energy associated with the spatial overlap of electron wavefunctions. The Heisenberg exchange Hamiltonian describes the effect of exchange interaction, which leads to the emergence of an effective magnetic field known as the exchange field ($\mathbf{H}_{\text{exchange}}$) [41].

$$\mathbf{H}_{\text{exchange}} = \frac{2A_{\text{ex}}}{\mu_0 M_{\text{s}}}\nabla^2 \mathbf{m} \tag{2.4}$$

where A_{ex} is the exchange stiffness constant.

2.2.3 Anisotropy Field

The magnetization in ferromagnetic materials often aligns preferentially along certain directions or shape anisotropy [41]. The magnetic anisotropy energy describes the dependence of energy on the orientation of the magnetization. The anisotropy field $\mathbf{H}_{\text{anis}}$ is the effective magnetic field resulting from the anisotropy energy. A large $\mathbf{H}_{\text{anis}}$ will align the magnetic moments along the easy axis of magnetization.

$$\mathbf{H}_{\text{anisotropy}} = -\frac{2K_u}{\mu_0 M_s}(\mathbf{m} \cdot \mathbf{u})\mathbf{u} \tag{2.5}$$

Here K_u denotes the anisotropy constant, $\mathbf{u}$ indicates the easy axis direction, and $\mathbf{m}$ is the unit vector of magnetization.

2.2.4 Dipolar Field

In magnetic materials, magnetic moments generate a magnetic field that interacts with neighboring magnetic moments, leading to dipole-dipole interactions and the formation of a dipolar field. The dipolar field $\mathbf{H}_{\text{dipolar}}$ at a specific point due to a single dipole with magnetic moment $\mathbf{m}$ located at position $\mathbf{r}_0$ which is given by:

$$\mathbf{H}_{\text{dipolar}}(\mathbf{r}) = \frac{\mu_0}{4\pi}\left[\frac{3(\mathbf{m} \cdot \hat{\mathbf{r}})\hat{\mathbf{r}} - \mathbf{m}}{|\mathbf{r} - \mathbf{r}_0|^3}\right] \tag{2.6}$$

where $\hat{\mathbf{r}} = \frac{\mathbf{r}-\mathbf{r}_0}{|\mathbf{r}-\mathbf{r}_0|}$ is the unit vector, and $|\mathbf{r} - \mathbf{r}_0|$ is the distance between source dipole to the observation point. The total dipolar field at a point is represented by:

$$\mathbf{H}_{\text{dipolar}}(\mathbf{r}) = \sum_i \mathbf{H}_{\text{dipolar},i}(\mathbf{r}) \tag{2.7}$$

where $\mathbf{H}_{\text{dipolar},i}(\mathbf{r})$ is the field due to the i-th dipole in the system.

2.2.5 Zeeman Field

The Zeeman field ($\mathbf{H}_{\text{Zeeman}}$) represents the influence of an external magnetic field $\mathbf{H}$.

$$\mathbf{H}_{\text{Zeeman}} = \mathbf{H} \tag{2.8}$$

where $\mathbf{H}$ denotes the external magnetic field, and this external field directly contributes to the total effective magnetic field. The corresponding Zeeman energy density = $-\mu_0 \mathbf{M} \cdot \mathbf{H}$, where $\mathbf{M}$ is the magnetization. The energy is minimized when the magnetization is aligned with the external field $\mathbf{H}$, however, if the magnetization is not aligned with the $\mathbf{H}$, then the energy will be increased.

2.2.6 Thermal Fluctuations

Thermal fluctuations introduce randomness into the magnetic materials, driven by thermal energy at non-zero temperatures [42]. These fluctuations can cause spontaneous magnetization reversals and significantly impact the stability of magnetic states. A stochastic component is added to the magnetic field to model thermal fluctuations and simulate the random thermal motion of magnetic moments. This approach is crucial for understanding magnetic material behavior in practical thermal conditions. The thermal field $\mathbf{B}_{\text{therm}}$ is given by:

$$\mathbf{B}_{\text{therm}} = \sqrt{\frac{2\mu_0 \alpha k_B T}{M_{\text{s}} |\gamma| \Delta V \Delta t}} \boldsymbol{\eta} \tag{2.9}$$

where α is the Gilbert damping parameter, k_B is the Boltzmann constant, T is the finite temperature, M_{s} is the saturation magnetization, $|\gamma|$ is the gyromagnetic ratio, ΔV is the volume element, Δt is the time step, and $\boldsymbol{\eta}$ represents a vector of random numbers which is normally distributed with a mean of zero and a unit variance. Thermal fluctuations were neglected in this thesis; however, including them would be an important next step.

2.3 Model and Method

Schematic Diagram

The schematic diagram in Fig. 2.1 illustrates the setup used in this thesis for the micromagnetic simulations of spin waves propagation in YIG microstrips, and typical material parameters are given in Table 2.1. The coordinate system is defined with the length l along the x-axis, width w along the y-axis, and thickness along the z-axis, where the thickness is a few microns. A static magnetic field $\mathbf{H}$ is applied within the xy plane at an angle of ϕ with respect to the x-axis. In this thesis, the same coordinate system is used throughout. Initially, $\mathbf{H}$ is applied at angle ϕ, and the system is relaxed to get an equilibrium state. The equilibrium state is such that the magnetization is mostly aligned along $\mathbf{H}$. After that, a dynamic field $\mathbf{H}_{\text{dyn}}$ is applied, and the dynamics response is simulated. This approach ensures that the system is stabilized before exciting the spin wave dynamics.

Fig. 2.1 (a) shows the YIG microstrip's top view with its dimensions, where the width (w) is less than the length (l). A stripline antenna, located at the center of the microstrip, is 50 μm wide (crosshatched area in Fig. 2.1 (a)). This antenna is used to apply the $\mathbf{H}_{\text{dyn}}$ along the x and z-axis to excite broadband spin wave dynamics, and the stripline antenna matches with experiment setup [1]. Fig. 2.1 (b) shows a point source excitations that create spin wave caustics. The $\mathbf{H}_{\text{dyn}}$ applied only to the z-axis, which is depicted at the center of the microstrip, and it is a diameter of 50 μm (i.e., crosshatch pattern circle). This point source represents a localized field excitation in the simulation. The simulations were conducted for three distinct positions of the point source, middle, top, and bottom, to compare to the stripline excitations.

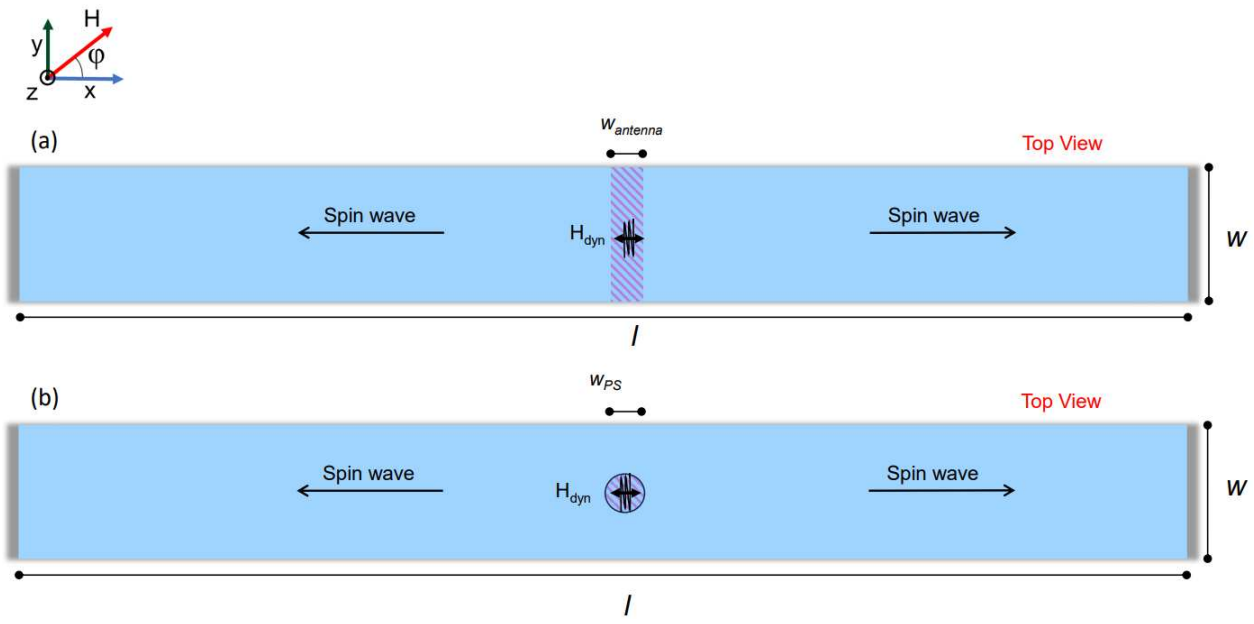

Figure 2.1: Schematic diagram of the layout used in the micromagnetic simulations. A static magnetic field **H** is applied in the xy plane for both the stripline antenna and the point source cases with a specific angle ϕ with respect to x-axis to align the magnetic moments in a preferred direction. The top view of the YIG illustrates its length (l), width (w), and thickness (not shown in the figure, i.e., pointing outside of the page) where $w << l$. (a) A stripline antenna, positioned in the middle of the sample, measures 50 μm, and a dynamic magnetic field $\mathbf{H}_{\text{dyn}}$ is applied along the x and z-axis. This excitation field can be either a sinc or sinusoidal function with respect to time. (b) The point source, located at the center of the microstrip (or can be located in the top or bottom position), has a diameter of 50 μm, analogous to the stripline antenna. The coordinate system in this figure will be used consistently for the rest of the thesis.

Table 2.1: The material parameters used for yttrium iron garnet (YIG) and other useful simulation parameters.

Name	**Symbol**	**Value**	**Unit**
Mesh Size	n	Variable	-
Cell Size	dx	Variable	m
Permeability of Free Space	μ_0	$4\pi \times 10^{-7}$	H/m
Gyromagnetic Ratio	$\lvert\gamma\rvert$	2.211×10^5	rad/(s T)
Saturation Magnetization	M_s	0.14×10^6	A/m
Exchange Stiffness	A_{ex}	4.2×10^{-12}	J/m
Damping Constant	α	Variable	-
External Magnetic Field	H_{ext}	Variable	A/m
Total Simulation Time	T	Variable	s

Sinc Pulse & Sinusoidal Pulse

A sinc pulse is used as an external magnetic field shown in Fig. 2.2 to excite the spin waves over a range of frequencies. The sinc pulse function is defined by the following equation:

$$\mathbf{H}_{\text{dyn}}(x, y, t) = \frac{\mathbf{h}_0(x, y)\sin(2\pi f_c(t - t_0))}{2\pi f_c(t - t_0)} \tag{2.10}$$

where $\mathbf{H}_{\text{dyn}}$ is the dynamic magnetic field strength, $\mathbf{h}_0$ is the amplitude of the sinusoidal magnetic field, and f_c is the sinc pulse frequency. The denominator $2\pi f_c(t - t_0)$ normalizes the sinusoidal function, ensuring the amplitude diminishes as t moves away from the initial time offset for a specific minima t_0.

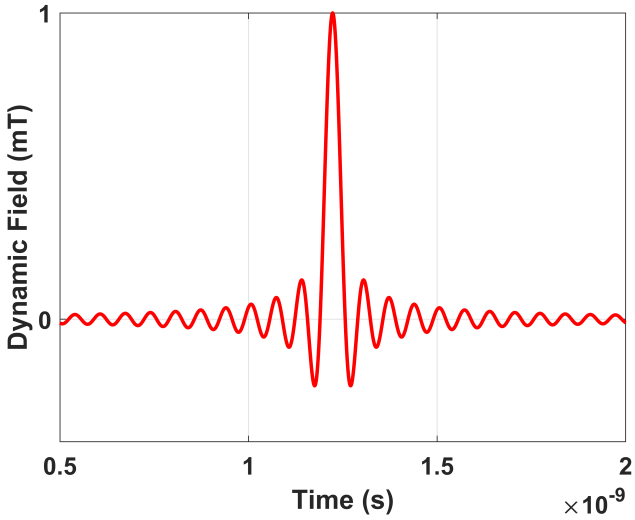

Figure 2.2: The parameters for the sinc pulse are as follows: pulse frequency (f_c) is 15 GHz, initial time offset for the 4^{th} minima (t_0) is 1223×10^{-12} seconds, and the magnetic field pulse amplitude ($\mu_0 h_0$) is 1 mT.

In this thesis, two primary spatial distributions $\mathbf{h}_0(x, y)$ are used shown in Fig 2.1. The first distribution is used to represent a stripline antenna shown in Fig. 2.1 (a). For the second distribution, a Gaussian function $f(x, y)$ is used to approximate a localized point source excitation shown in Fig. 2.1 (b).

For the stripline antenna, we define the spatially varying external magnetic field components B_x, B_y, and B_z derived using the Biot-Savart law for a sheet current of width w_a. The magnetic field components $B_x(x)$, $B_y(x)$, and $B_z(z)$ are given as follows:

$$\begin{aligned} B_x(x) &= B_0 \frac{\left(\arctan\left(\frac{x+a}{z_p}\right) - \arctan\left(\frac{x-a}{z_p}\right)\right)}{2\arctan\left(\frac{a}{z_p}\right)} \\ B_y(x) &= 0 \\ B_z(x) &= B_0 \frac{1}{2} \log\left(\frac{z_p^2 + (x-a)^2}{z_p^2 + (x+a)^2}\right) \frac{1}{2\arctan\left(\frac{a}{z_p}\right)} \end{aligned} \tag{2.11}$$

where $a = \frac{w_a}{2}$ is the half-width of the antenna, and $w_a = 50$ μm. The height of the antenna is $z_p = 5$ μm. The magnetic field above the center of the antenna (at x = 0) is defined as $B_0 = \mu_0 h_0 = 0.05$ mT, in which $\mu_0 = 4\pi \times 10^{-7}$ H/m denotes the magnetic permeability in a vacuum, and h_0 represent magnetic field amplitude. The field distribution in Eq. 2.10 for a microstrip antenna antenna is hence:

$$\mathbf{h_0} = \frac{1}{\mu_0} \left(B_x(x), 0, B_z(x)\right) \tag{2.12}$$

By applying the Biot-Savart law, we can accurately simulate the magnetic field in the region above the antenna, taking into account the geometry and current distribution.

To obtain images of the spin wave propagation patterns, the simulation is run using the sinusoidal excitation until a steady state response is reached, typically for 400 periods. The magnetization is saved at equal time increments over the last period of the simulation. The function $\mathbf{h}_0(x, y) \cdot g(t)$ was used to generate traveling waves. Here, $\mathbf{h}_0(x, y)$ describes the spatial distribution of properties, while $g(t)$ models its temporal evolution. In our case, we use:

$$g(t) = \sin(2\pi f t) \tag{2.13}$$

where f is the spin wave driving frequency.

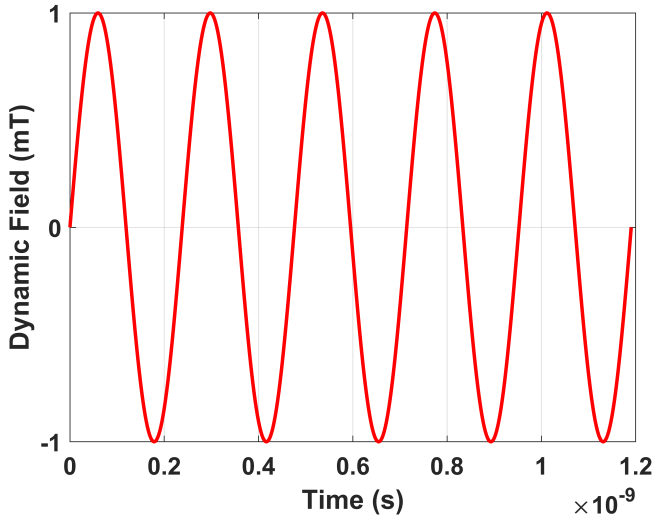

Figure 2.3: The spin wave driving frequency f is 4.2 GHz, and magnetic field pulse amplitude $\mu_0 h_0$ is 1 mT.

For the point source, a Gaussian distribution was used to model the spatial variation of the magnetic field. This approach provides a realistic representation of localized magnetic excitations. The mathematical form of the Gaussian distribution used in these simulations is given by:

$$\mathbf{h}_0(x, y) = \frac{B_0}{\mu_0} \exp\left(-\frac{(x - x_0)^2 + (y - y_0)^2}{2\sigma^2}\right) \hat{z} \tag{2.14}$$

where B_0 is the amplitude of the magnetic field, (x_0, y_0) is the center of the Gaussian distribution, and σ = 50 μm is the standard deviation, which controls the width of the distribution. The dynamic magnetic field was applied in the z-direction. This setup ensures that the magnetic field strength decreases smoothly and symmetrically away from the center point in the x and y directions and produces a localized excitation.

Chapter 3

Analysis of Spin Wave Simulations

3.1 Simulations of Dispersion Relations

In order to understand the spin wave dispersion relations, sinc pulse simulations were conducted, in which a magnetic dynamic field was applied to the time-varying excitation field shown in Eq. 2.10. Generally, a sinc pulse produces a broad range of frequencies in the YIG microstrip, and these frequencies excite the magnetic material and create the spin waves that propagate along the axis of the microstrip. Analysis of these simulations yields the spin wave dispersion relation, and the spin wave dispersion relations are used to select specific driving frequencies for further study. The YIG magnetic parameters for the simulations with a sinc pulse excitation were obtained from Ref. [1]. The microstrip specifications for the sinc pulse: length of $l = 40.96$ μm, width $w = 1.28$ μm, thickness $t = 0.01$ μm, antenna width $w_{\text{antenna}} = 2.01$ μm, pulse amplitude $\mu_0 h_0 = 1$ mT, pumping frequency $f_c = 15$ GHz, Gilbert damping parameter $\alpha = 0.001$, saturation magnetization $M_{\text{s}} = 0.14 \times 10^6$ A/m, exchange stiffness $A_{\text{ex}} = 4.2 \times 10^{-12}$ J/m, shown in Table 2.1. A static magnetic field $\mathbf{H} = 0.087$ T applied in-plane with $\phi = 90^\circ$ with respect to the x-direction, which is called surface wave configuration. The simulations run for a duration of 10 ns.

Figure 3.1 shows the normalized magnetization dynamics components m_x, m_y, and m_z over a period of 10 ns in response to the sinc pulse excitation. The m_x and m_z components show an abrupt onset of the dynamics followed by damped oscillations. At the same time, m_y remains nearly constant (Fig. 3.1 (b)) because the static magnetic field is applied in the y direction. The magnetic moments are magnetized primarily along the y-axis with a slight tilt at the edges, which is called the flower state [11]. The magnetic moments are free to precess in the perpendicular directions to the static magnetization, hence we see oscillations in m_x and m_z shown in Figs. 3.1 (a) and 3.1 (c), respectively.

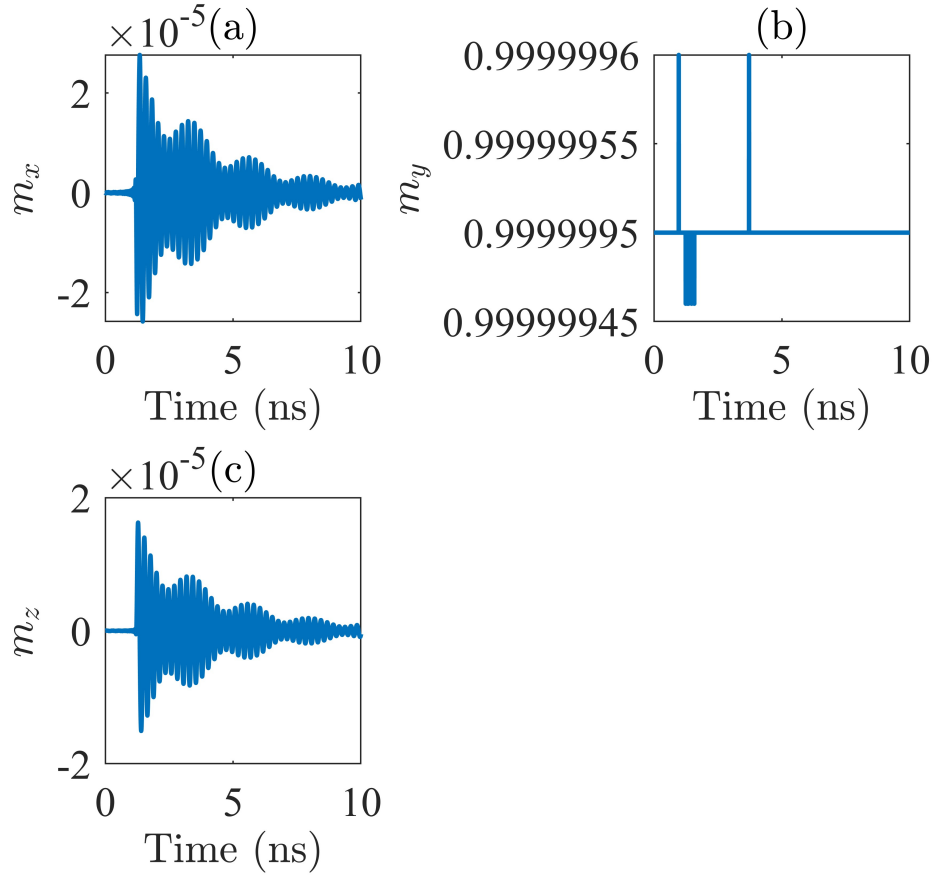

Figure 3.1: Normalized magnetization components m_x, m_y, and m_z as functions of time. The solid blue lines represent the dynamic response over time. The m_x and m_z components in (a) and (c), respectively, exhibit oscillatory behavior with decreasing amplitude centered around zero, while (b) shows that m_y remains nearly constant at around 0.9999995.

Fourier analysis was performed on the simulation output results to obtain the spin wave excitation frequencies and the dispersion relations. Fig. 3.2 shows the interpolation of the normalized magnetization components m_x, m_y, and m_z as functions of time t. Since MuMax3 simulations use an adaptive time step, the data points are not evenly spaced. Interpolation is performed to create a fixed time base that is required for the Fast Fourier Transform (FFT) algorithm. The close alignment between original and interpolated data confirms the accuracy of the interpolation, which is essential for performing Fourier analysis using the FFT algorithm.

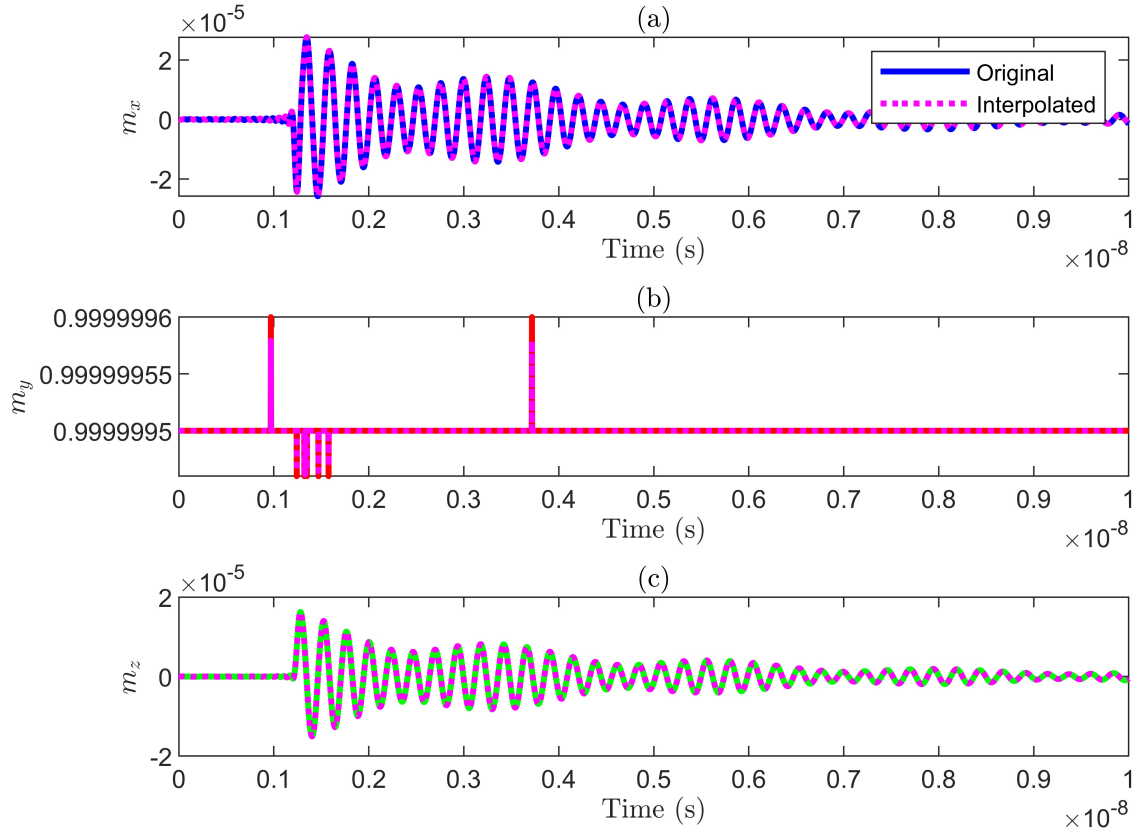

Figure 3.2: Figure illustrates the normalized magnetization dynamics over a simulation run time of 10 ns. (a), (b), and (c) show the normalized magnetization components m_x, m_y, and m_z as functions of time t, respectively. The solid lines represent the original magnetization dynamics; the dotted lines represent the interpolated dynamics. The interpolation is applied to create a fixed time base that is required for the fast Fourier transform (FFT) algorithm.

3.1.1 Fast Fourier Transform (FFT) Analysis

A Fast Fourier transform (FFT) analysis was performed first to determine the frequency range of the spin waves. Then, following the method outlined in Copus et al., [11] to find the spin wave dispersion relations.

Fig. 3.3 presents the FFT analysis of the normalized magnetization components m_x, m_y, and m_z as functions of frequency. Fig. 3.3 (a) shows the m_x component, which has a primary peak around 4.2 GHz with an amplitude of approximately 0.035. As shown in Fig. 3.3 (c), the m_z

component also features a primary peak around 4.2 GHz with an amplitude of approximately 0.018, almost half of the amplitude of m_x shown in Fig. 3.3 (a). The m_x amplitude response is approximately double with respect to the m_z amplitude response because there is a stronger demagnetization restoring force acting on out-of-plane tilt in a thin film.

Fig. 3.3 (b) depicts the m_y component, which exhibits a lower amplitude on the order of 10^{-6} because the m_y component is essentially static. In Fig. 3.3 (a), and Fig. 3.3 (c), a secondary peak present at $\approx$ 3.72 GHz that may indicate higher-order modes. This analysis shows that spin waves are excited most strongly at $\approx$ 4.2 GHz, and oscillations primarily involve the m_x and m_z components, which are expected.

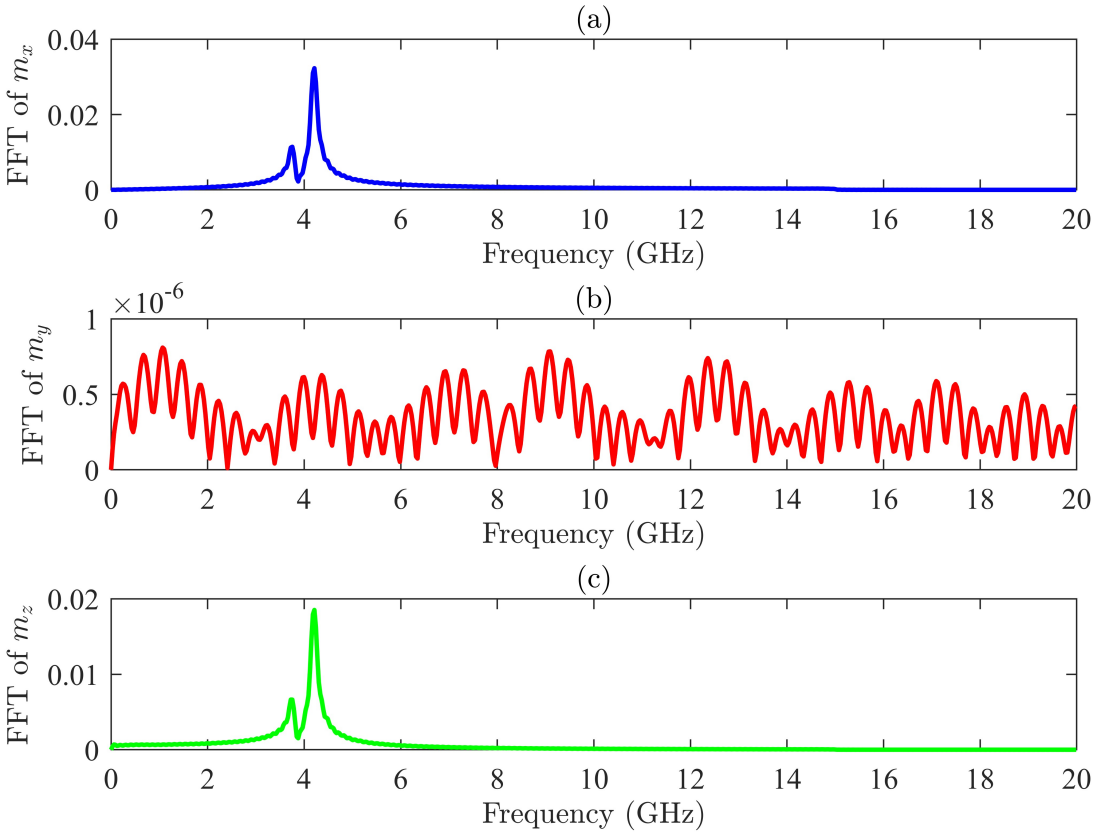

Figure 3.3: Fast Fourier Transforms (FFTs) of the normalized magnetization components m_x, m_y, and m_z shown in Fig. 3.2 as a function of frequency. (a) The m_x component shows a primary peak $\approx$ 4.2 GHz, with an amplitude of $\approx$ 0.035. (b) The m_y component exhibits significantly lower amplitudes since the m_y response is essentially static with minimal dynamic response. (c) The m_z component also displays a primary peak $\approx$ 4.2 GHz, similar to m_x; however, the amplitude is almost half of that found in (a).

Fig. 3.4 illustrates the magnetization m_z as a function of x and t for a YIG microstrip with a length of 40.96 μm, a width of 1.28 μm, and a thickness of 0.01 μm, the same microstrip considered in Fig. 2.1, and Table 2.1. The antenna was positioned at the center of the microstrip, and the static magnetic field direction was set to $\phi = 90°$. This plot shows the variation of the magnetization component m_z as a function of time t and position x. The color map represents the magnitude of m_z over time with a scale ranging from -1 to 1 (the same color maps will be used for the rest of the section, and the oscillations are normalized to the maximum value). The magnetization oscillations are most prominent at the center of the plot, as well as the antenna's location. As

time passes, the oscillations that originate at the antenna propagate outward along the x-axis. The waveform is strong at the center, diminishes as it moves toward the edges, and dissipates before reaching the edges of the microstrip. The damping parameter was selected carefully to obtain a reasonable propagation distance but with no reflections.

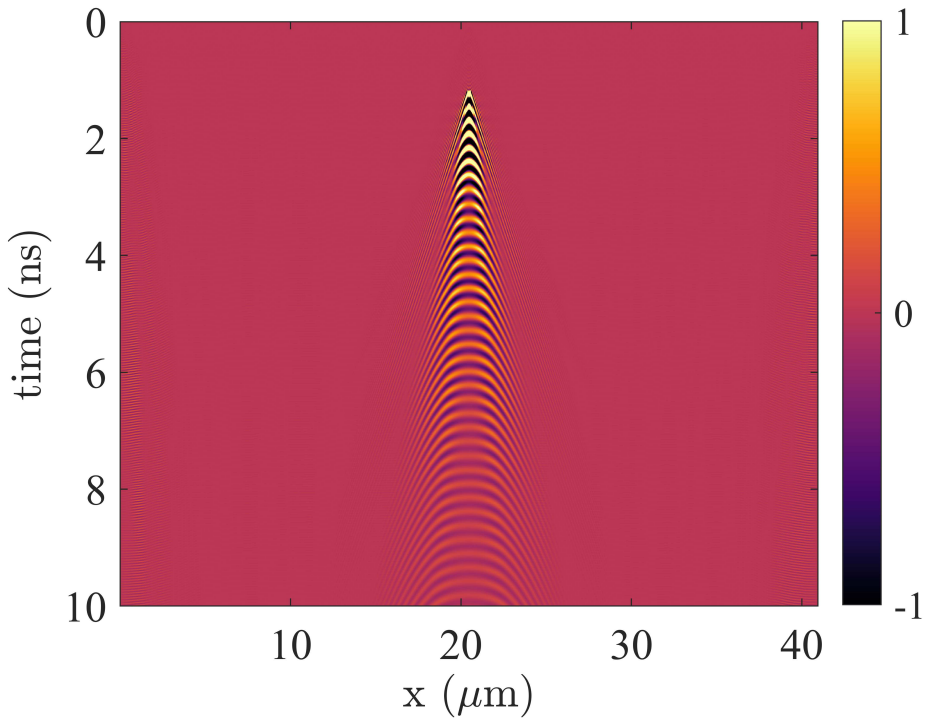

Figure 3.4: Magnetization m_z as a function of x and t (at y = 0.64 μm, the center of microstrip) for a YIG microstrip with a length of 40.96 μm, a width of 1.28 μm, and a thickness of 0.01 μm. The color map indicates the magnitude of m_z over a time period with values where the color scale ranges from -1 to 1. The central region shows prominent magnetization oscillations that propagate outward over time, and the spin wave dissipates before reaching the microstrip edges.

3.1.2 Spin Wave Dispersion Relations

The two-dimensional Fourier transform of Fig. 3.4 produces the dispersion relation shown in Fig. 3.5, which can be compared to the dispersion relation [11]. The dispersion relation also shows how spin wave frequencies vary with the wave vector in the microstrip. The central bright region indicates a spin wave excitation region with frequencies concentrated around 4 GHz to 6 GHz, where the wave vectors should be close to 0 μm ($k > 0$). The parabolic shape of the bright

region (smiley face) is characteristic of spin wave dispersion relations for YIG in the magnetostatic surface wave (MSSW) configuration where the static magnetic field direction is $\phi = 90°$, and $\mathbf{H}$ is perpendicular to k. In the MSSW configuration, the frequency f goes up with increasing wave vector k.

The dispersion relation provides a critical insight into the behavior of spin waves in the YIG microstrip. By examining the dispersion relation, one can easily identify the specific frequency or frequency ranges and the corresponding wave vectors that can excited. For instance, in Fig. 3.5, the central bright region in the dispersion plot indicates the dominant spin wave modes with frequencies concentrated above approximately 4 GHz where wave vectors are nearly zero. This information provides a layout for selecting an appropriate driving frequency for the experiment technique or simulation technique that lies within the antenna's broadband range. The dispersion relation in Fig. 3.5 was used to select a driving frequency of 4.2 GHz, indicated by the horizontal solid green line, for further investigation, and the fainter parabolas at successively higher frequencies are higher order width-quantized modes.

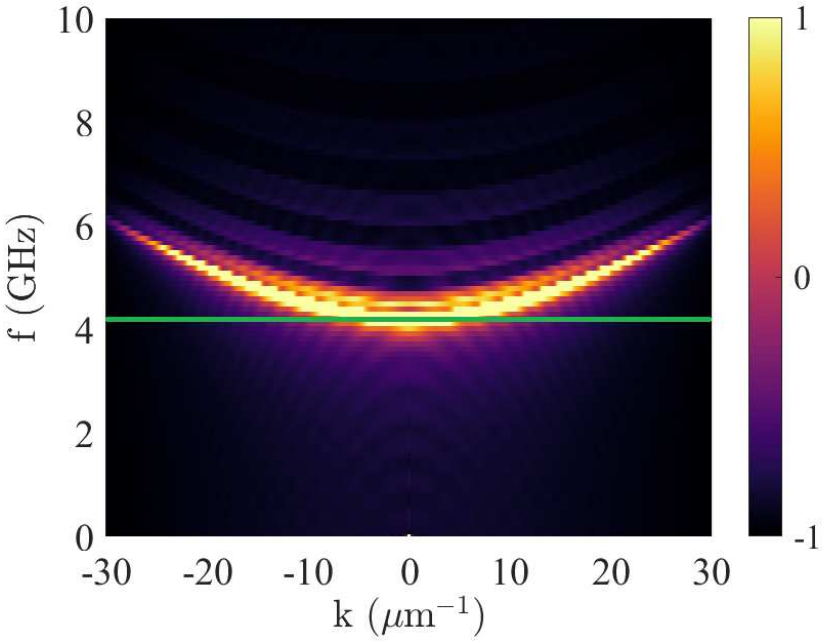

Figure 3.5: Spin wave dispersion relation for a YIG microstrip, showing the wave vector k vs. frequency f. The central bright region indicates a spin wave excitation region with frequencies concentrated around 4 GHz to 6 GHz. The parabolic shape of the spin wave dispersion relation typical for spin waves in YIG in the MSSW configuration with **H** is perpendicular to the wave vector k ($\phi = 90°$).

Fig 3.6 shows the same dispersion relation for spin waves in a YIG microstrip with the same parameters as in Fig. 3.5 but with a horizontal axis of the wave vector, k multiplied by the thickness dz, where kdz is dimensionless. This representation can be used to determine how spin waves will behave in thin films for a broad range of thicknesses. This is important because larger thicknesses were used for the spin wave-driven simulations and point source excitation simulations.

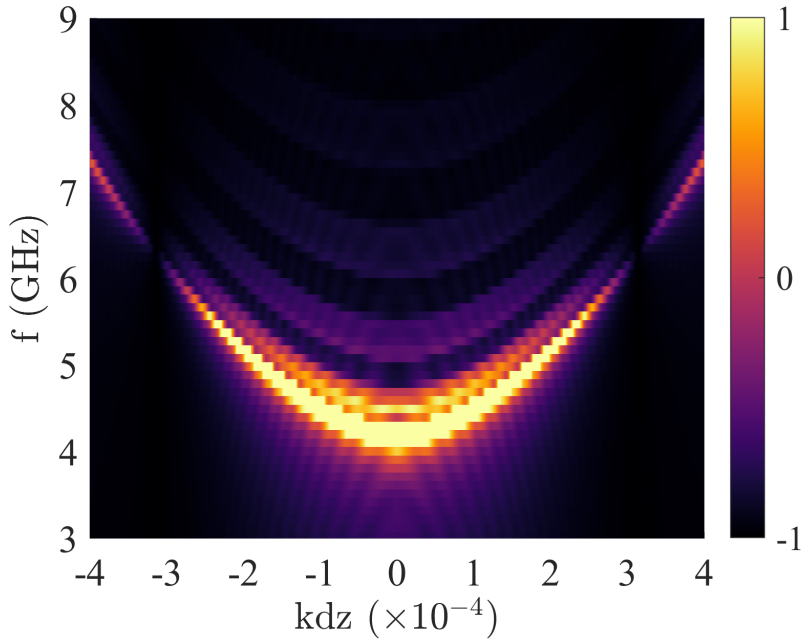

Figure 3.6: Spin wave dispersion relations for a YIG microstrip. The horizontal axis represents the wave vector k multiplied by the thickness dz, where kdz is dimensionless. The plot shows prominent modes between 4 GHz and 8 GHz.

It is important to note that the magnetic dispersion relations depend on the material parameters and geometry. In general, increasing the width of the microstrips results in more closely spaced width-quantized spin wave modes, making the dispersion relation appear more continuous whereas decreasing the width leads to greater mode separation, so typically only one mode is excited at a given frequency [43].

3.2 Spin Wave Driven Dynamics

The goal of driven simulations is to visualize the spin wave patterns at specific frequencies. These patterns can then be compared to experimental results.

3.2.1 Temporal Dynamics of Magnetization Components

Fig. 3.7 shows the normalized, spatially averaged, magnetization components m_x, m_y, and m_z for a YIG microstrip in response to a sinusoidal excitation. The simulations ran for 400 time

periods (i.e., 95.24 ns). After that, the 401st period was saved out to create movies of the spin wave propagation. Over that time, the sinusoidal patterns reach a steady state where the amplitude and phases of the magnetic oscillations settle to constant values. Here are the specifications of a microstrip made of YIG: length $l = 3276.8$ μm, width $w = 409.6$ μm, thickness $t = 6$ μm, antenna width $w_{\text{antenna}} = 50$ μm, pulse amplitude $\mu_0 h_0 = 5$ mT, driving frequency $f = 4.2$ GHz (selected using Fig. 3.5), damping parameter $\alpha = 0.005$, saturation magnetization $M_{\text{s}} = 0.14 \times 10^6$ A/m, exchange stiffness $A_{\text{ex}} = 4.2 \times 10^{-12}$ J/m and static magnetic field applied $\mathbf{H} = 0.087$ T at an angle of $\phi = 70°$ with respect to the x-direction.

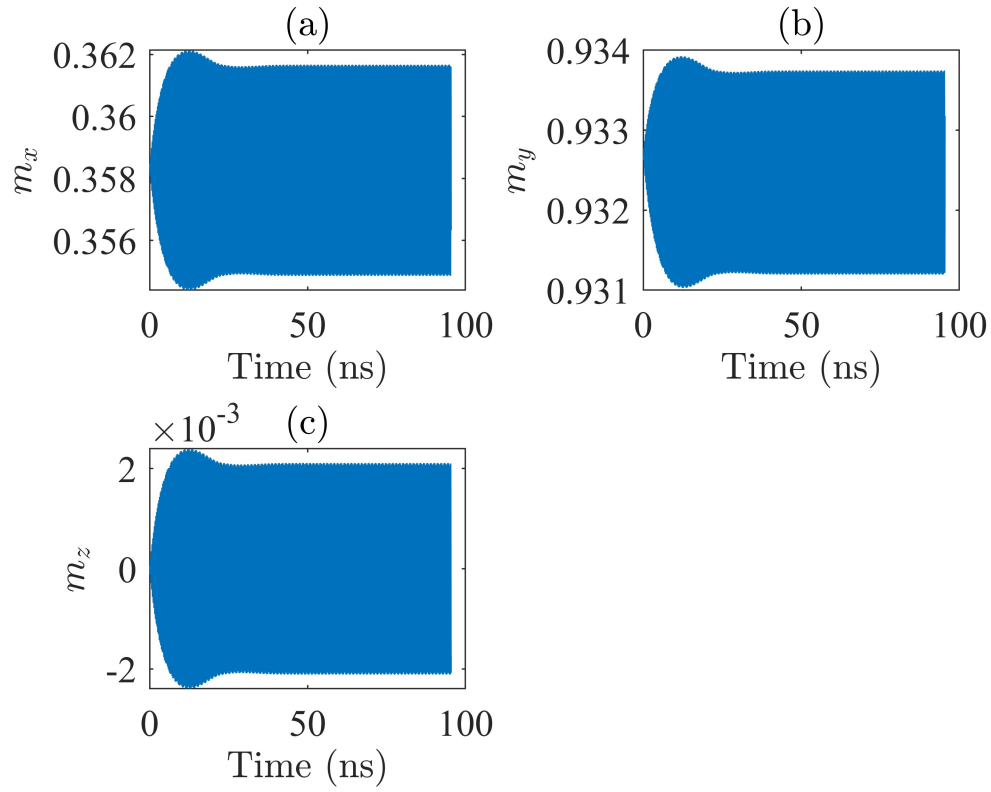

Figure 3.7: Normalized magnetization components m_x, m_y, and m_z. The simulation reaches steady-state behavior after approximately 40 ns. Microstrip specifications: length $l = 3276.8$ μm, width $w = 409.6$ μm, thickness $t = 6$ μm, antenna width $w_{\text{antenna}} = 50$ μm, pulse amplitude $\mu_0 h_0 = 5$ mT, driving frequency $f_c = 4.2$ GHz, damping parameter $\alpha = 0.005$, saturation magnetization $M_{\text{s}} = 0.14 \times 10^6$ A/m, exchange stiffness $A_{\text{ex}} = 4.2 \times 10^{-12}$ J/m and static magnetic field applied $\mathbf{H} = 0.087$ T at an angle of $\phi = 70°$ with respect to the x-direction.

3.2.2 Damping Dependency Spin Wave Propagation

In this section, we observed how the damping parameter dictated the spin wave propagation in YIG materials. YIG was selected because of its low magnetic damping and long spin wave propagation distances in the microstrip, and the real value for α is approximately 2.2×10^{-4} [6,44]. However, using this low value in simulations is impractical because spin waves will reflect from the boundary, and it takes too long to reach a steady state response. We ran simulations with different values of α in order to select a reasonable value to balance various considerations, such as the boundary reflections and proper spin-wave propagation in the microstrip antenna.

Figs. 3.8, and 3.9 show spin wave snapshots as a function of the angle in YIG microstrip, where length $l = 3276.8$ μm, width $w = 409.6$ μm, thickness $t = 6$ μm, antenna width $w_{\text{antenna}} = 50$ μm (i.e., the antenna was placed in the middle of the microstrip through out this thesis for stripline antenna cases), pulse amplitude $\mu_0 h_0 = 1$ mT, driving frequency $f = 4.2$ GHz, damping parameter $\alpha = 0.001$ (i.e., lower damping shown in Fig. 3.8), and $\alpha = 0.005$ (i.e., higher damping shown in Fig. 3.9), saturation magnetization $M_{\text{s}} = 0.14 \times 10^6$ A/m, exchange stiffness $A_{\text{ex}} = 4.2 \times 10^{-12}$ J/m and static magnetic field applied $\mathbf{H} = 0.087$ T at an angle of $\phi = 70^\circ$ with respect to the x-direction.

In the case of $\alpha = 0.001$, Fig. 3.8, the spin waves propagate further along the total length of the microstrip because of the very low damping as compared to Fig. 3.9, and spin waves hit the edges, reflect back, and interfere with the main pulse. Therefore, it is hard to distinguish the main beam pulse and the reflected beam pulse. Also, the pixelation of the images indicates that the simulation cell size may not adequately capture all of the detailed information. The cell size could be decreased to solve this, however, the chosen cell size should be sufficient to capture the wavelengths of interest provided the simulations are kept within the linear range. The other approach, used here, is to reduce alpha and/or $\mathbf{H}$ to ensure the simulations are within the linear regime. The static magnetic field directions are 70°, 80°, 90°, and the spin wave propagation patterns look like more tilted diamonds, tilted diamonds, and diamonds, respectively. The color map represents the magnitude of the M_z component of the magnetization. The scale ranges from Mz_{min} (represented

by black color) to Mz_{max} (represented by yellow color), where $Mz_{\text{min}} = -Mz_{\text{max}}$. The same color map is used for all of the snapshot maps throughout this thesis.

To reduce the reflections and the pixelation issues, a larger damping coefficient $\alpha = 0.005$ and a smooth magnetic field profile for the antenna were used Eq. 2.11. In Fig. 3.9, the spin wave propagation is remarkably improved. There are no signs of reflections at the edges of the microstrip compared to the $\alpha = 0.001$ case, and the spin waves are no longer pixelated. The 90° static magnetic field orientation produced a distinct diamond pattern, yielding promising results that align well with our experimental observations [1]. As the ϕ is reduced from 90° to 70°, the diamond patterns tilt, also in agreement with the experiment.

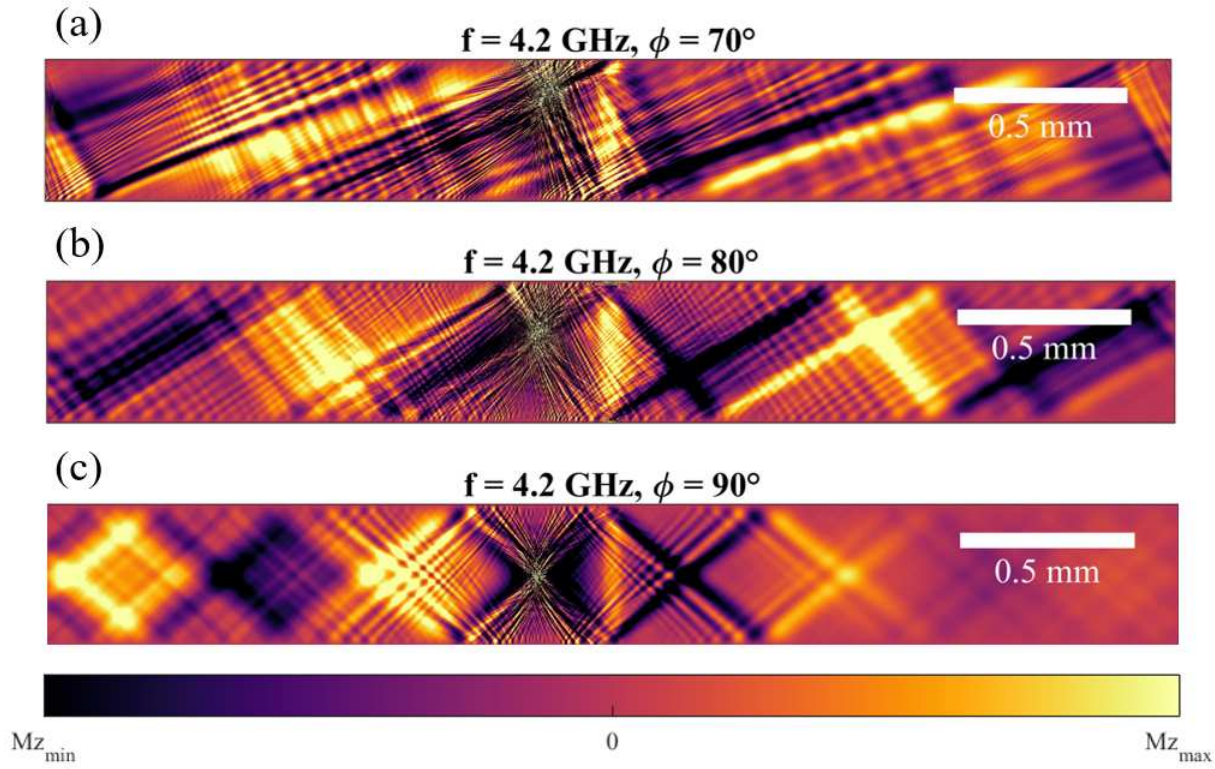

Figure 3.8: Spin wave snapshots of movie where the parameters are: length $l = 3276.8$ μm, width $w = 409.6$ μm, thickness $t = 6$ μm, antenna width $w_{\text{antenna}} = 50$ μm (i.e., the antenna was placed in the middle of the microstrip throughout this thesis for stripline antenna cases), pulse amplitude $\mu_0 h_0 = 1$ mT, driving frequency $f = 4.2$ GHz, the damping parameter $\alpha = 0.001$, saturation magnetization $M_{\text{s}} = 0.14 \times 10^6$ A/m, exchange stiffness $A_{\text{ex}} = 4.2 \times 10^{-12}$ J/m and static magnetic field applied $\mathbf{H} = 0.087$ T at angles of $\phi = 70°$, $80°$, and $90°$ with respect to the x-direction. The antenna field is applied along the x and z axes in Eq. 2.11. The color map represents the magnitude of the M_z component of the magnetization. The scale ranges from Mz_{min} (represented by black color) to Mz_{max} (represented by yellow color). The same color map is used for all the snapshot maps throughout the thesis.

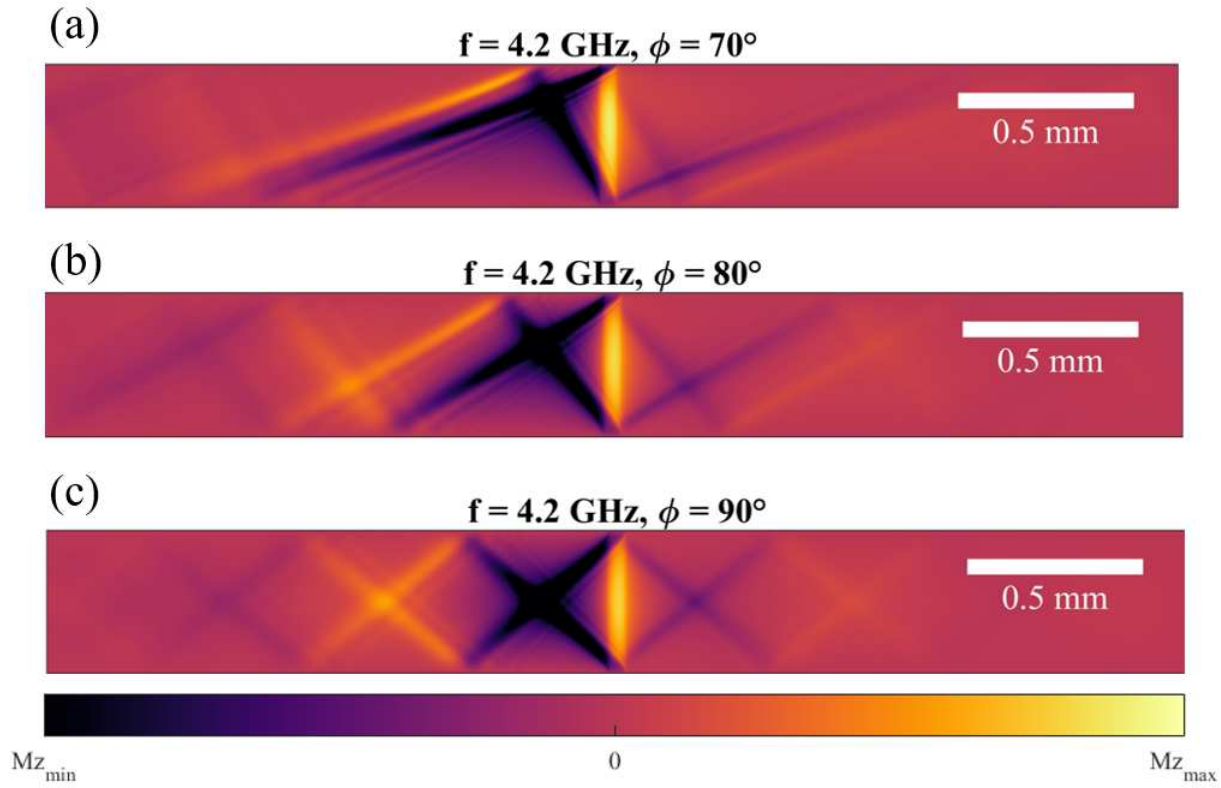

Figure 3.9: Spin wave snapshots of movie where the parameters are: length $l = 3276.8$ μm, width $w = 409.6$ μm, thickness $t = 6$ μm, antenna width $w_{\text{antenna}} = 50$ μm, pulse amplitude $\mu_0 h_0 = 1$ mT, driving frequency $f = 4.2$ GHz, damping parameter $\alpha = 0.005$, saturation magnetization $M_{\text{s}} = 0.14 \times 10^6$ A/m, exchange stiffness $A_{\text{ex}} = 4.2 \times 10^{-12}$ J/m and static magnetic field applied $\mathbf{H} = 0.087$ T at angle of $\phi = 70°$, $80°$ and $90°$ with respect to the x-direction. The antenna is located in the middle of the microstrip antenna, and the antenna field equation is shown in Eq. 2.11. For the larger damping, there are no observable reflections at the boundary as the spin waves dissipate before reaching it, preventing any return reflections within the microstrip.

Figs. 3.10, and 3.11 show spin wave intensity maps as a function of angle where spin wave propagation in the YIG material with a low damping parameter $\alpha = 0.001$, and higher damping parameter $\alpha = 0.005$. These intensity maps corresponded to the mode snapshots in Figs. 3.8, and 3.9 respectively. The color scale ranges from 0 to the maximum value of $\langle M_z \rangle$, highlighting the areas of intense spin wave activity, and the same color map is used for all the spin wave intensity maps throughout this thesis. These intensity maps are highly valuable as they can be directly compared to Brillouin light scattering experiments (BLS), which vividly explain the experimental results.

The intensity maps (Figs. 3.10 and 3.11) show the same main features as the corresponding mode snapshots (Figs. 3.8, and 3.9, respectively). The damping parameter $\alpha = 0.005$ will be used for the rest of the thesis, except in Section 3.2.4 ($\alpha = 0.01$).

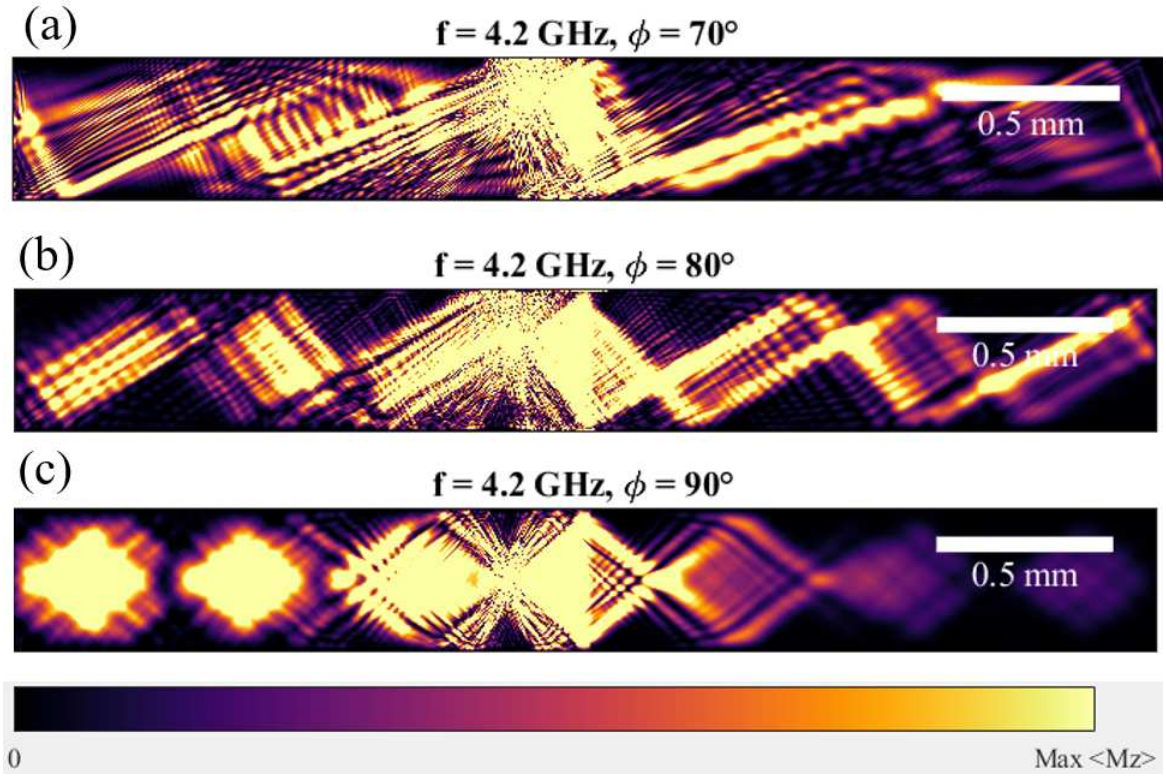

Figure 3.10: Spin wave intensity maps with $\alpha = 0.001$ at $f = 4.2$ GHz and $\mathbf{H} = 0.087$ T, taken at $\phi = 70°$, $80°$, and $90°$ are shown in (a), (b), and (c) respectively. The microstrip specifications are (same as Fig. 3.8): length $l = 3276.8$ μm, width $w = 409.6$ μm, thickness $t = 6$ μm, and antenna width $w_{\text{antenna}} = 50$ μm. The antenna is located at the center of the microstrip. The color scale bar represents the amplitude of the magnetization component $\langle M_z \rangle$, with darker colors indicating lower intensity and brighter colors indicating higher intensity, highlighting areas of intense spin wave activity. The same color map is used for all the intensity maps throughout this thesis.

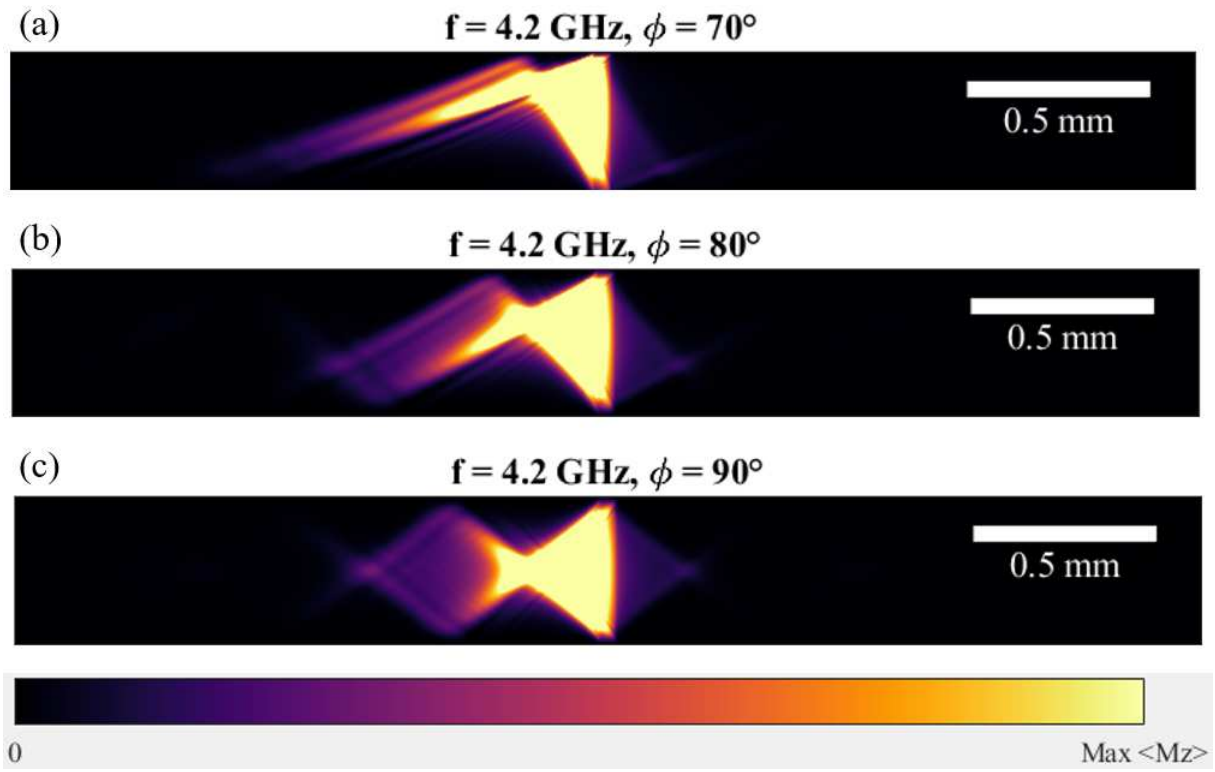

Figure 3.11: Spin wave propagation intensity maps with $\alpha = 0.005$ at $f = 4.2$ GHz and $\mathbf{H} = 0.087$ T, taken at $\phi = 70°$, $80°$, and $90°$ are shown in (a), (b), and (c) respectively. The microstrip specifications are (same as Fig. 3.9): length $l = 3276.8$ μm, width $w = 409.6$ μm, thickness $t = 6$ μm, and antenna width $w_{\text{antenna}} = 50$ μm. This figure shows no reflections after hitting the boundary edges.

3.2.3 The Effects of Driving Frequency on Spin Waves

Spin waves are sensitive to the applied static magnetic field direction, as shown in from Figs. 3.8 to 3.11 but they also depend on frequency. In this section, we investigated the spin wave frequency dependence in the YIG microstrip using sinusoidal excitations. We observed subtle changes in the spin wave propagation patterns by adjusting the excitation frequencies between $f = 4.2$ GHz and 4.3 GHz.

Analysis at 4.2 GHz and 4.3 GHz Frequencies

Figs. 3.12 and 3.13 present snapshots and intensity maps of spin wave propagation in a YIG with a damping parameter ($\alpha = 0.005$) at driving frequencies of $f = 4.2$ GHz and 4.3 GHz respectively, under a static magnetic field $\mathbf{H} = 0.087$ T. These spin wave snapshots and maps

were calculated at three different static magnetic field orientations, $\phi = 70°$, $80°$, and $90°$. The microstrip used in the simulations has dimensions of length $l = 3276.8$ μm, width $w = 409.6$ μm, thickness $t = 6$ μm, and antenna width $w_{\text{antenna}} = 50$ μm.

The mode snapshots in Fig. 3.12 are somewhat difficult to compare when the frequency changes. The intensity maps shown in Fig. 3.13 are easier to compare. In Fig. 3.13 (a), at an angle of $70°$, the spin wave patterns exhibit subtle differences between the two frequencies. For 4.2 GHz, the interference pattern is a more spread-tilted diamond shape, whereas for 4.3 GHz, the pattern becomes less spread out tilted diamond is observed for both cases, but the diamond vertices are close to the antenna at 4.3 GHz. In Fig., 3.13 (b), at $80°$, 4.2 GHz shows a pattern that exhibited a tilted diamond shape with a high-intensity outline, while 4.3 GHz shows a tilted diamond-shaped interference which is a smaller change compared to the effective static field. In Fig. 3.13 (c), at $90°$, the diamond patterns become even clear, with 4.2 GHz, and showing a sharp, confined diamond pattern. However, 4.3 GHz displays a similar but less spread-out pattern. Therefore, these comparisons highlight how slight changes in frequency and magnetic field orientation can significantly affect spin wave propagation and interference patterns.

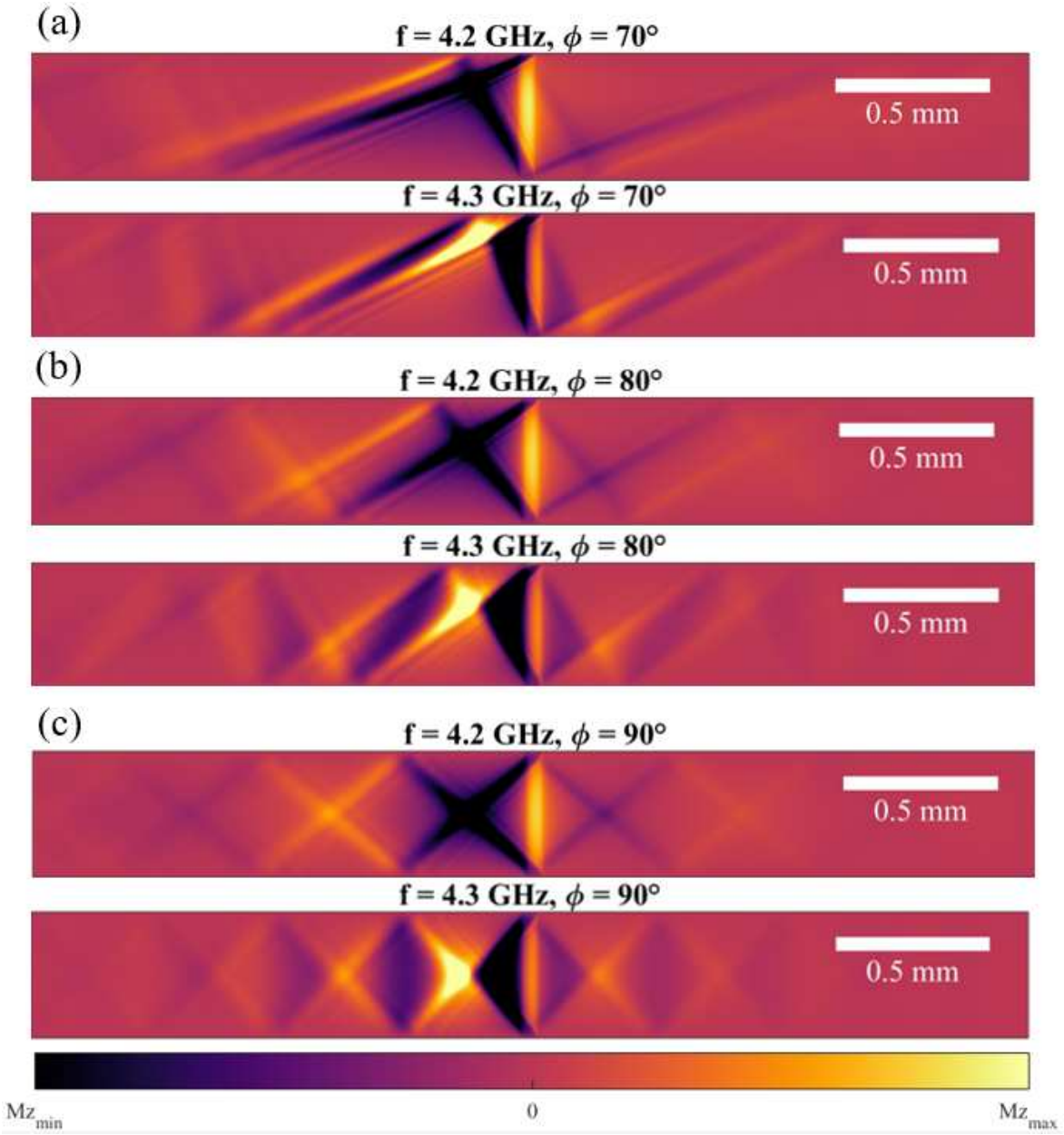

Figure 3.12: Snapshots of spin wave propagation with a damping parameter $\alpha = 0.005$ at driving frequencies of $f = 4.2$ GHz and 4.3 GHz, taken at orientations of $\phi = 70°$, $80°$, and $90°$, length $l = 3276.8$ μm, width w = 409.6 μm, thickness t = 6 μm, and antenna width $w_{\text{antenna}} = 50$ μm, and static magnetic field $\mathbf{H} = 0.087$ T.

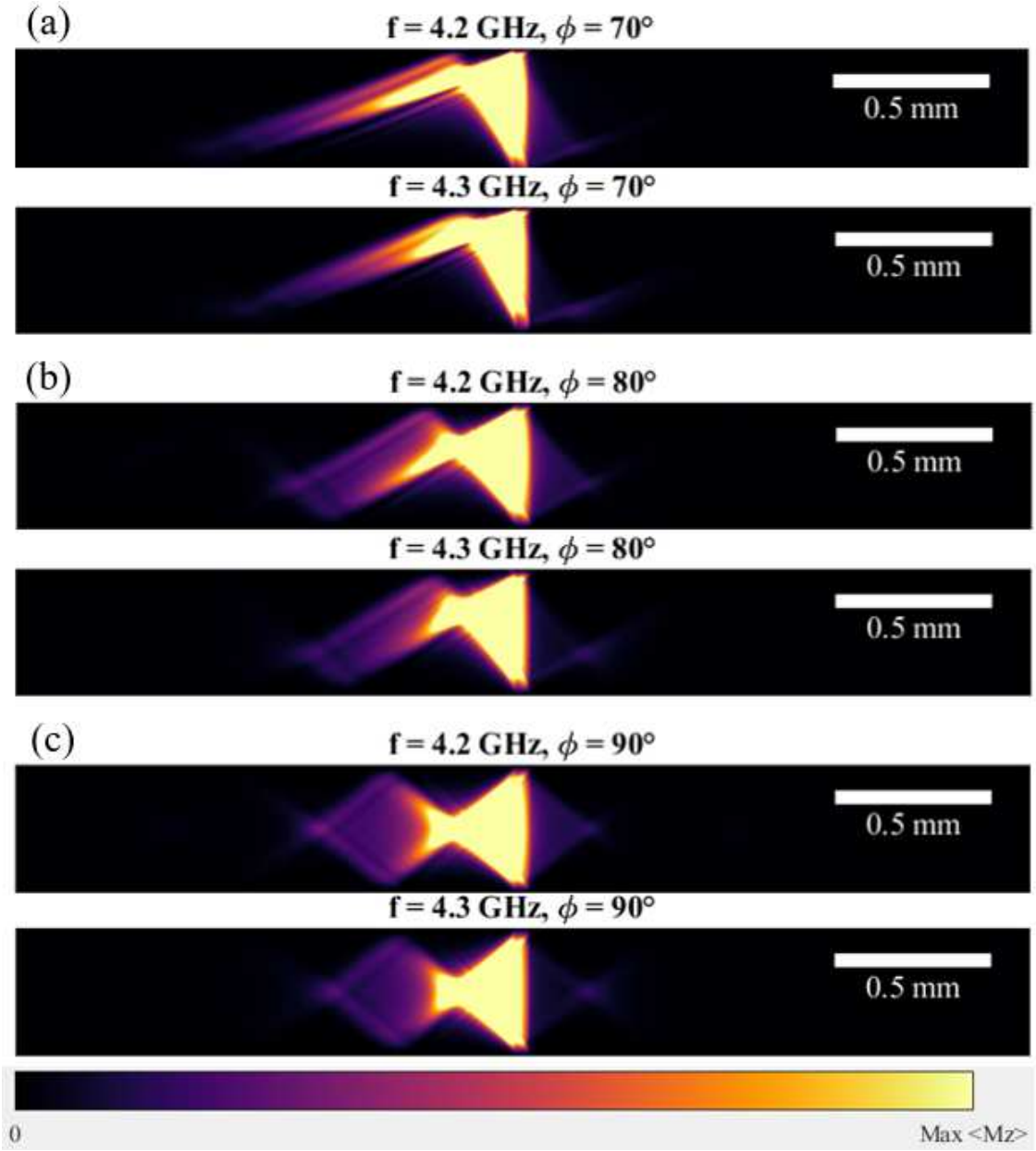

Figure 3.13: Intensity maps of spin wave propagation with a damping parameter $\alpha = 0.005$ at driving frequencies of $f = 4.2$ GHz and 4.3 GHz, taken at orientations of $\phi = 70°$, 80°, and 90°, length $l = 3276.8$ μm, width w = 409.6 μm, thickness t = 6 μm, and antenna width $w_{\text{antenna}} = 50$ μm, and static magnetic field $\mathbf{H} = 0.087$ T.

3.2.4 Nonreciprocity of Spin Wave Propagation

Magnetostatic surface spin waves exhibit nonreciprocity, that is asymmetric propagation of spin waves where the spin wave amplitude or phase differs for waves that travel in opposite direc-

tions. The orientation of the static magnetic field can alter the spin wave propagation directions and the amplitude non-reciprocity. Fig. 3.14 displays mode snapshots, and Fig. 3.15 shows the corresponding spin wave intensity maps for spin wave propagation in YIG. The microstrip parameters are length $l = 3276.8$ μm, width $w = 409.6$ μm, thickness $t = 6$ μm, and antenna width $w_{\text{antenna}} = 50$ μm, damping coefficient $\alpha = 0.01$ (i.e., considering larger damping), driven at a frequency of $f = 4.2$ GHz, and the static magnetic field $\mathbf{H} = 0.087$ T. The left columns in Figs. 3.14, and 3.15 show mode snapshots and intensity maps, respectively, for the static magnetic field orientations $\phi = 70°$, $80°$, and $90°$, while the right columns show results for field orientations $\phi = 250°$, $260°$, and $270°$. Figs. 3.14, and 3.15 both show nonreciprocity which means the left side has a higher intensity compared to the right, or vice versa. For spin waves, the direction of high intensity is reversed when the magnetic field direction is reserved. Additionally, the phases of the spin waves on the left side and right side are mirror images, and everything is flipped. This effect is well known for surface spin waves, i.e., for $\phi = 90°$, and $270°$. These simulations demonstrate that non-reciprocity also holds for angles of up to $\pm$ $20°$ from the MSSW configuration.

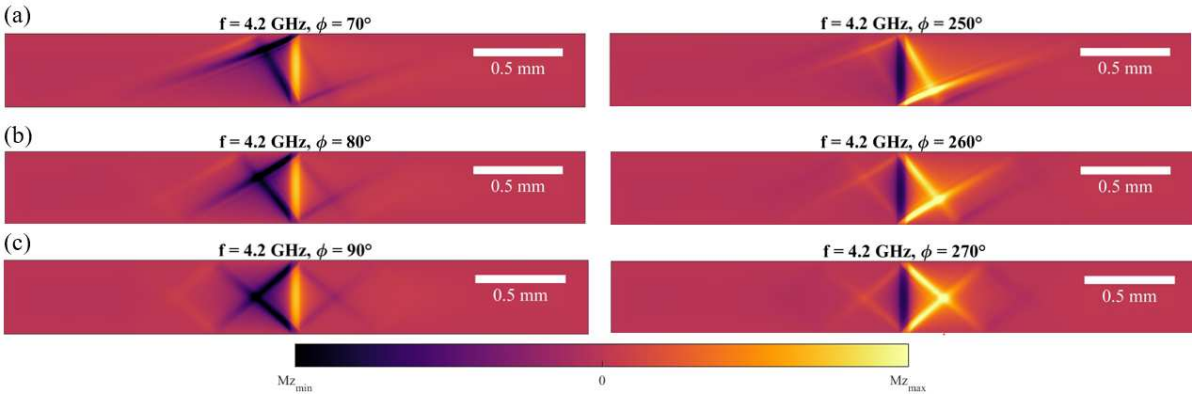

Figure 3.14: Snapshots simulations with a damping parameter $\alpha = 0.01$ (i.e., considering larger damping), driving frequency of $f = 4.2$ GHz, static magnetic field orientations $\phi = 70°$, $80°$, $90°$ (left) and $\phi = 250°$, $260°$, $270°$ (right). The microstrip specifications are length $l = 3276.8$ μm, width $w = 409.6$ μm, thickness $t = 6$ μm, and antenna width $w_{\text{antenna}} = 50$ μm with a static magnetic field of $\mathbf{H} = 0.087$ T. The all of the snapshots are taken here at the same time. The antenna is located at the center of the microstrip. The intensity shows that reversing the field direction by $180°$ results in mirrored symmetry in spin-wave propagation.

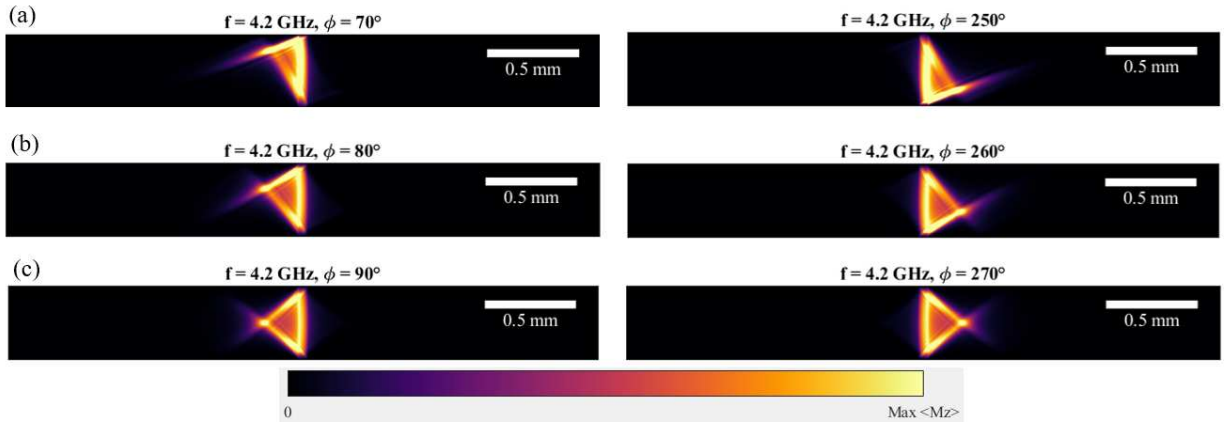

Figure 3.15: Intensity maps from simulations with a damping parameter $\alpha = 0.01$ (i.e., considering larger damping), driving frequency of $f = 4.2$ GHz, static magnetic field orientations $\phi = 70°, 80°, 90°$ (left) and $\phi = 250°, 260°, 270°$ (right). The microstrip specifications are length $l = 3276.8$ μm, width $w = 409.6$ μm, thickness $t = 6$ μm, and antenna width $w_{\text{antenna}} = 50$ μm with a static magnetic field of $\mathbf{H} = 0.087$ T. The antenna is located at the center of the microstrip. The intensity shows that reversing the field direction by $180°$ results in mirrored symmetry in spin-wave propagation.

3.2.5 Spin Wave Width Quantization

Simulations were done as a function of microstrip width to understand the effect of the spin wave width quantization. Figs. 3.16, and 3.17 shows mode snapshots and intensity maps from simulations of spin wave propagation in YIG with a damping parameter $\alpha = 0.005$, driven at a frequency of $f = 4.2$ GHz with a static magnetic field $\mathbf{H} = 0.087$ T at static field orientations of $\phi = 70°, 80°$, and $90°$. Microstrip widths of $w = 0.4096$ mm, $w = 0.2048$ mm, and $w = 0.1024$ mm were considered while the thickness remains constant at $t = 6$ μm.

At $\phi = 70°$ tilted, the spin wave patterns show a well-defined tilted diamond pattern with well-defined boundaries ($w = 0.4096$). This pattern is due to the presence of many width-quantized modes. The pattern boundary becomes less well defined/smoother as the width decreases, and the decrease in width also corresponds to fewer modes. For the narrowest strip ($w = 0.1024$ mm), the patterns become simple, and smooth because only one width-quantized mode is excited. At $\phi = 80°$ for a moderately tilted diamond case, a simple trend is observed. The widest strip exhibits a diamond-shaped interference pattern, which becomes simpler as the width decreases. The patterns become simple and diffuse for $w = 0.1024$ mm, and the diamond patterns resemble a

snake. At $\phi = 90^\circ$ for the diamond case, the spin wave patterns are also complex (many modes) for the widest strip ($w = 0.4096$ mm) and become less complex (fewer modes) as the width decreases. For the narrowest strip ($w = 0.1024$ mm), simplest case, the diamond shape becomes a circular dotted shape in the mode snapshot and a single, central streak in the intensity map that decreases in intensity with increasing distance from the antenna.

As the width is decreased, the separation in the k of the width quantized modes increases, since $\Delta k_\omega = \frac{\pi}{w}$. As a consequence, fewer width quantized modes can be excited for smaller w. This leads to smoother observed patterns for decreasing w, as shown in Fig. 3.17. At $\phi = 90^\circ$, the widest strip shows strong and clear diamond patterns that occur due to the interference of the width-quantized modes [15]. As the width is reduced, especially at $w = 0.1024$ mm, the patterns become simpler. Interestingly, for smaller width w, $\phi = 90^\circ$, the intensity maps appear to exhibit a single mode with no intensity modulation. In contrast, for $\phi = 70^\circ$ and 80°, the maps reveal a snake-like back-and-forth beam pattern, which is likely due to a single mode that reflects back and forth from the sample edges as it travels. In order for this to occur, the group velocity must be at a non-zero angle with respect to x.

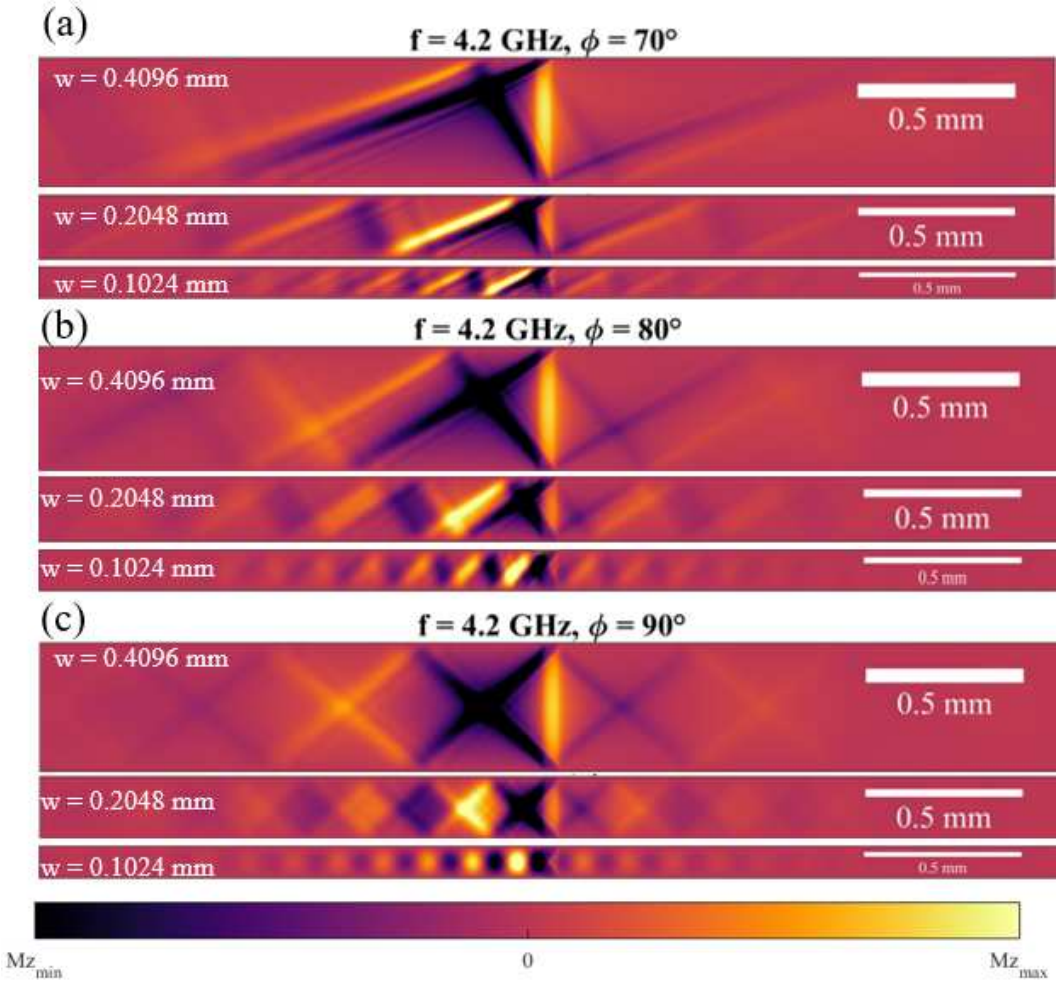

Figure 3.16: Snapshots from simulations with a damping parameter $\alpha = 0.005$ at a driving frequency of $f = 4.2$ GHz, taken at orientations of $\phi = 70°$, $80°$, and $90°$. The microstrip widths are $w = 0.4096$ mm, $w = 0.2048$ mm, and $w = 0.1024$ mm, with a constant thickness of 6 μm and a static magnetic field $\mathbf{H} = 0.087$ T. The images show that as the width decreases, the interference patterns become less complex. At $w = 0.1024$ mm, the narrowest width, the patterns are the simplest.

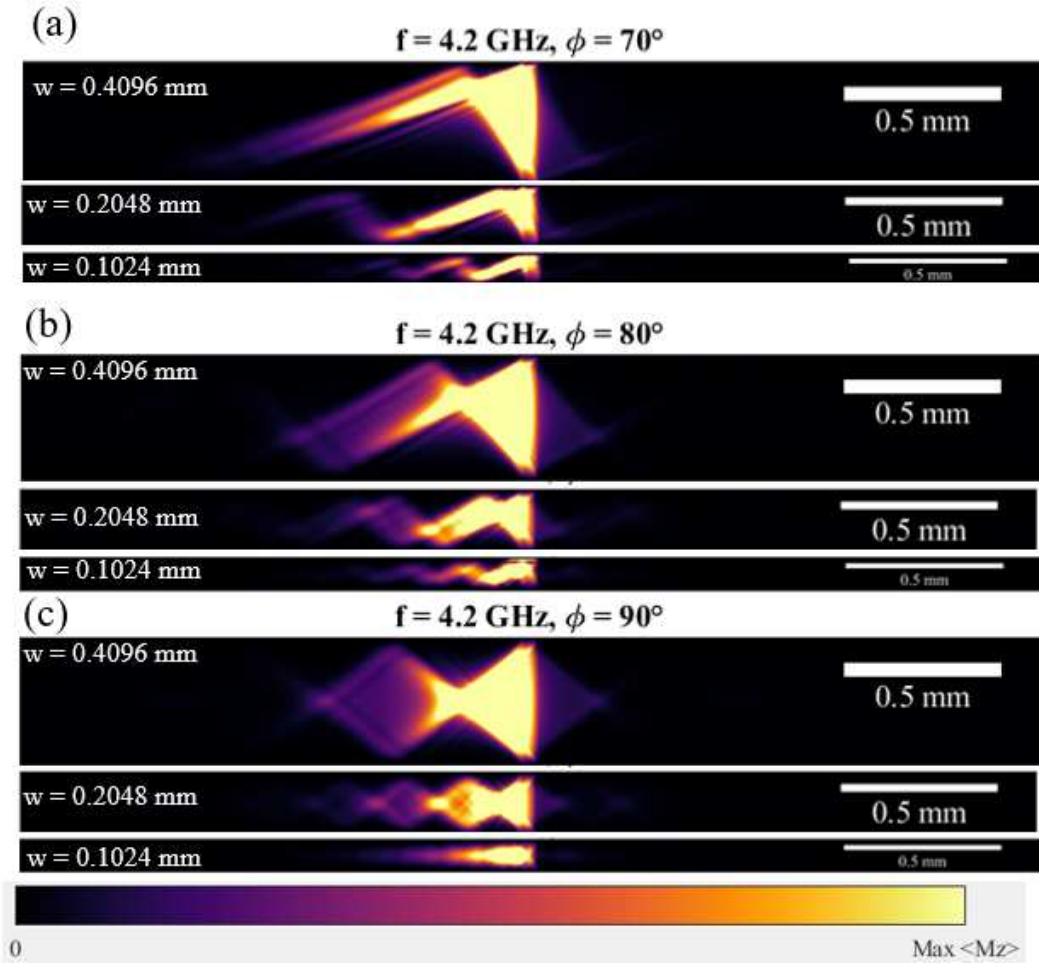

Figure 3.17: Intensity maps from simulations with a damping parameter $\alpha = 0.005$ at a driving frequency of $f = 4.2$ GHz, taken at orientations of $\phi = 70°$, $80°$, and $90°$. The microstrip widths are $w = 0.4096$ mm, $w = 0.2048$ mm, and $w = 0.1024$ mm, with a constant thickness of 6 μm and a static magnetic field $\mathbf{H} = 0.087$ T. The images show that as the width decreases, the interference patterns become less complex. For $\phi = 70°$, $80°$ cases, the simpler mode shows snake back-and-forth patterns for $w = 0.1024$ mm.

3.3 Point Source Simulation Studies

The goal of studying localized spin wave generation using a point source in micromagnetic simulations is to understand the dynamics of spin wave propagation in a highly controlled situation.

A Gaussian spatial distribution was used to define the spatial variation of the dynamic magnetic field in the x and y axes, which excites the spin waves by perturbing the local magnetization, causing the spins to precess around the direction of the static magnetic field and generate the spin

waves. This point source setup allows us to generate caustic spin wave beams, which can then be compared to the diamond pattern obtained using a microstrip antenna.

The microstrip specifications for the point source simulations are as follows: length $l = 3276.8$ μm, width $w = 409.6$ μm, thickness $t = 6$ μm, the diameter of point sources of $w_{\text{PS}} = 50$ μm, pulse amplitude $\mu_0 h_0 = 0.05$ mT, driving frequency $f = 4.2$ GHz, damping parameter $\alpha = 0.005$, the saturation magnetization $M_{\text{s}} = 0.14 \times 10^6$ A/m, and the exchange stiffness $A_{\text{ex}} = 4.2 \times 10^{-12}$ J/m. The static magnetic field applied $\mathbf{H} = 0.0865$ T at an angle of $\phi = 70°, 80°$, and $90°$ with respect to the x-direction. The simulations were run for a duration of 400 periods to reach a steady state, and then the magnetization was saved out periodically over the course of one additional period.

3.3.1 Effect of Point Source Position: Top, Bottom, and Middle

Figs. 3.18 and 3.19 illustrate the results of spin wave propagation in YIG, with the spin waves generated by a point source positioned at three different locations: top, middle, and bottom. Fig. 3.18 shows mode snapshots that capture the temporal evolution of the spin waves, and Fig. 3.19 shows the corresponding spin wave intensity maps, that highlight the spatial distribution of the spin waves intensities for each source position. The point sources in the three different cases generated spin wave caustics [18, 19, 45], which are highly directional (i.e., transport energy preferentially direction) and excitation frequency dependent.

In Figs. 3.18 (a) and 3.18 (c), the point sources positioned at the top and bottom create multiple secondary beams that are hitting the width edges and come back to microstrip again and die out before reaching the long axis's boundary edges, and there are no reflections. The intensity maps in Fig. 3.19 illustrate distinct patterns of spin wave propagation based on the point source position. When positioned at the top Fig. 3.19 (a) and bottom Fig. 3.19 (c), the point sources generate directional caustics that propagate through the microstrip and die out before reaching the boundaries. In contrast, Fig. 3.18 (b) shows the point source in the middle, which generates caustics that also form the outline of a diamond through successive reflections. In terms of intensity, the

central point source Fig. 3.19 (b) produces a symmetric diamond-shaped pattern after reflecting from the edges. This comparison highlights how the source positioning significantly influences the spin wave patterns in the microstrip.

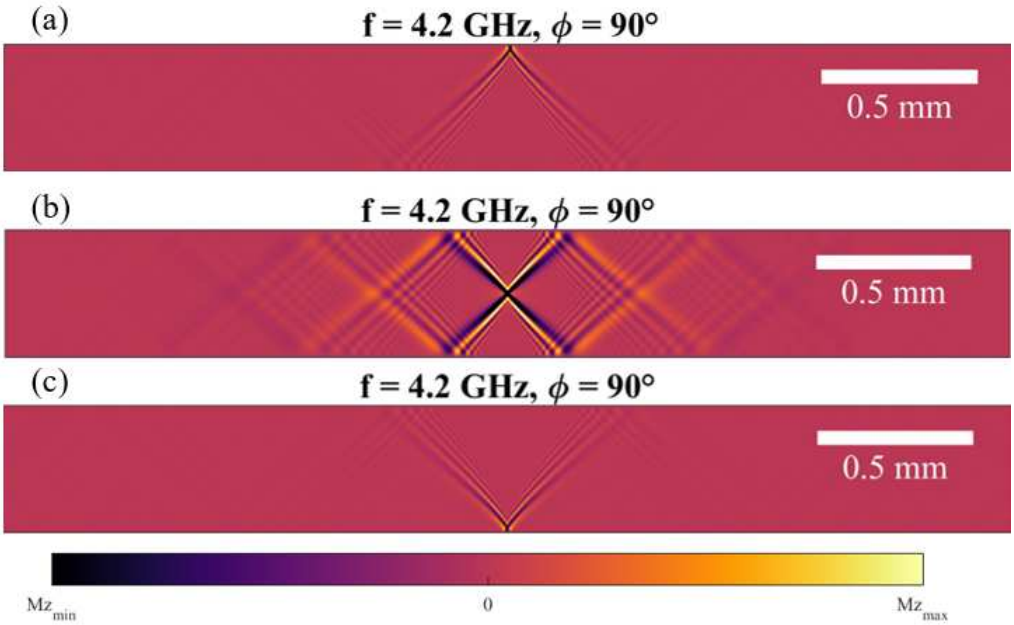

Figure 3.18: Snapshots from simulations of spin wave propagation in a magnetic material generated by a point source positioned at three different locations: top, middle, and bottom. Simulations parameters: length $l = 3276.8$ μm, width $w = 409.6$ μm, thickness $t = 6$ μm, the diameter of point sources of $w_{\text{PS}} = 50$ μm, pulse amplitude $\mu_0 h_0 = 0.05$ mT, driving frequency $f = 4.2$ GHz, damping parameter $\alpha = 0.005$, the saturation magnetization $M_{\text{s}} = 0.14 \times 10^6$ A/m, and the exchange stiffness is $A_{\text{ex}} = 4.2 \times 10^{-12}$ J/m. The static magnetic field applied $\mathbf{H} = 0.0865$ T at an angle of $\phi = 70°, 80°$, and $90°$ with respect to the x-direction.

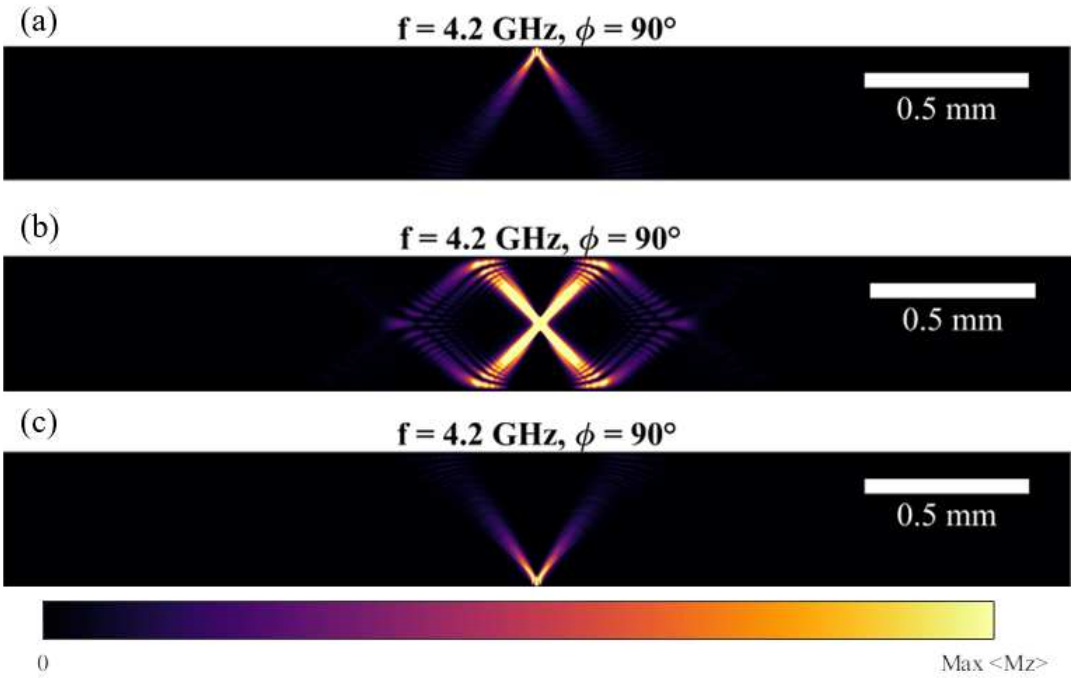

Figure 3.19: Intensity maps from simulations of spin wave propagation in a magnetic material generated by a point source positioned at three different locations: top, middle, and bottom. Simulation parameters: length $l = 3276.8$ μm, width $w = 409.6$ μm, thickness $t = 6$ μm, the diameter of point sources of $w_{\text{PS}} = 50$ μm, pulse amplitude $\mu_0 h_0 = 0.05$ mT, driving frequency $f = 4.2$ GHz, damping parameter $\alpha = 0.005$, the saturation magnetization $M_{\text{s}} = 0.14 \times 10^6$ A/m, and the exchange stiffness is $A_{\text{ex}} = 4.2 \times 10^{-12}$ J/m. The static magnetic field applied $\mathbf{H} = 0.0865$ T at an angle of $\phi = 70°, 80°$, and $90°$ with respect to the x-direction.

Fig. 3.20 displays spin wave intensity maps from simulations of spin wave propagation for three different driving frequencies when the point source is located in the middle of the microstrip: Fig. 3.20 (a), $f = 4.1$ GHz; Fig. 3.20 (b), $f = 4.2$ GHz; and Fig. 3.20 (c), $f = 4.3$ GHz. The simulations are conducted under a static magnetic field **H** = 0.0865 T applied at an angle of $\phi = 70°$ with respect to the x-direction, with a damping parameter of $\alpha = 0.005$. The point source excitation in the middle creates four distinct angles at the intersection point, labeled as θ_1, θ_2, θ_3, and θ_4 shown in Fig. 3.20 (a). The angle of spin wave caustic depends on the driving frequency and the direction of the static magnetic field. In Fig. 3.20, the static magnetic field is fixed, and the caustic angles, θ_1, θ_2, θ_3, and θ_4, change due to changes in the driving frequency. In Fig. 3.20 (a)

at $f = 4.1$ GHz, the intersecting spin wave beams form angles of $\theta_1 = 92°$, $\theta_2 = 88°$, $\theta_3 = 92°$, and $\theta_4 = 88°$.

The caustic angle is the angle difference between the static magnetic field direction ϕ and the initial beam direction θ_i shown in Fig. 3.21 (d). To calculate the caustic angle θ_c from Fig. 3.20 (a) for $\phi = 70°$ and a driving frequency of $f = 4.1$ GHz, we start with the static magnetic field direction, which is 70° from the long axis of the microstrip (x-axis). After that, we measure the initial beam angle from the x-axis, which is 25°. The caustic angle θ_c is the difference between these two angles, giving us $\theta_c = 45°$, as shown in Table 3.1. The spin wave caustics angles θ_c (ϕ with respect to **H**) are 45°, 43°, and 40° for driving frequencies of $f = 4.1$ GHz, 4.2 GHz, and 4.3 GHz, respectively. As the driving frequency increases, the caustics angle decreases, as summarized in Table 3.1.

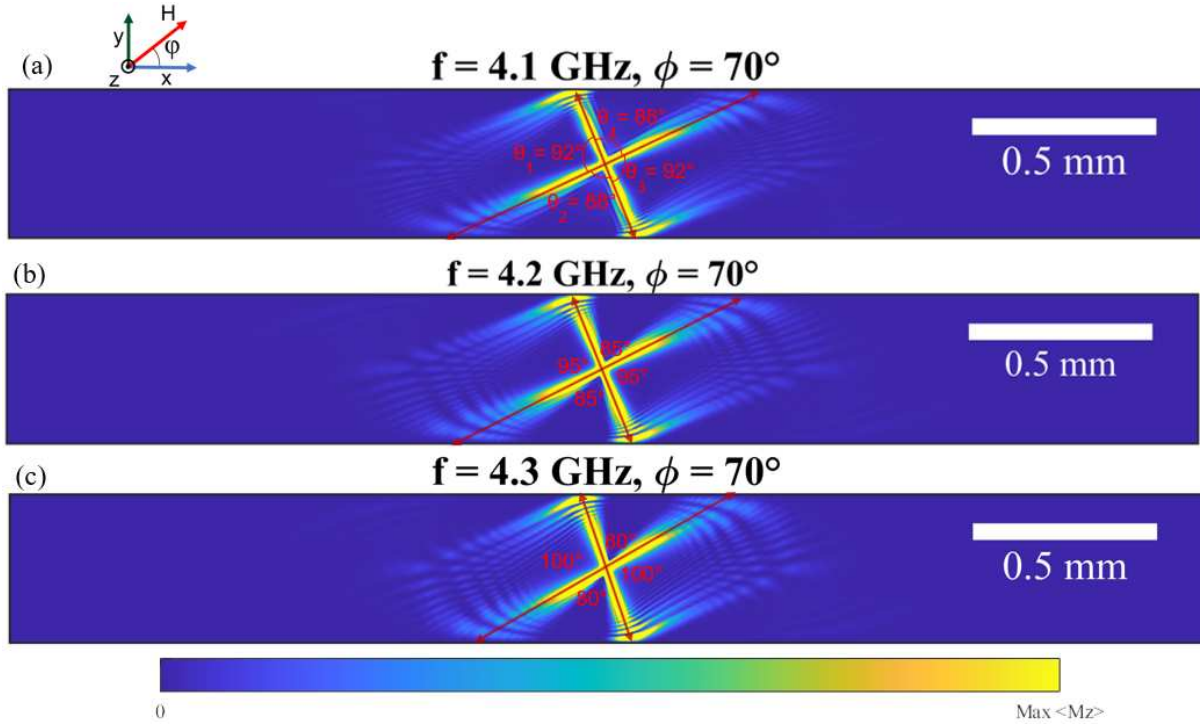

Figure 3.20: Intensity maps from simulations with a damping parameter $\alpha = 0.005$ at driving frequencies of $f = 4.1$ GHz (a), $f = 4.2$ GHz (b), and $f = 4.3$ GHz (c), with $\phi = 70°$. The dimensions of microstrip are length $l = 3276.8$ μm, width $w = 409.6$ μm, and thickness $t = 6$ μm, and the static magnetic field **H** is 0.0865 T. The point source excitation creates four angles at the intersection point, defined as $\theta_1 = 92°$, $\theta_2 = 88°$, $\theta_3 = 92°$, and $\theta_4 = 88°$. The images show frequency-dependent spin wave patterns with intersection angles marked in red.

Table 3.1: Static magnetic field direction, $\mathbf{H}$ (ϕ) at $\phi = 70°$, $80°$, and $90°$, driving frequencies, f(GHz), and corresponding pulse angles (θ_1, θ_2, θ_3, and θ_4), and spin-wave caustics angle, θ_c (ϕ with respect to $\mathbf{H}$)

Magnetic field direction, $\mathbf{H}(\phi)$	Driving frequency, f(GHz)	θ_1	θ_2	θ_3	θ_4	θ_c
70°	4.1	92°	88°	92°	88°	45°
70°	4.2	95°	85°	85°	95°	43°
70°	4.3	100°	80°	100°	80°	40°
80°	4.1	90°	90°	90°	90°	45°
80°	4.2	94°	86°	94°	86°	44 °
80°	4.3	100°	80°	100°	80°	39 °
90°	4.1	90°	90°	90°	90°	43°
90°	4.2	93°	87°	93°	87°	42°
90°	4.3	100°	80°	100°	80°	39°

Table 3.1 provides a summary of the relationship between the static magnetic field direction $\mathbf{H}$, driving frequencies f, corresponding pulse angles (θ_1, θ_2, θ_3, and θ_4), and the spin wave caustics angle θ_c, static magnetic field directions are $70°$, $80°$, and $90°$. For each magnetic field direction, the table lists the pulse and caustic angles for driving frequencies of 4.1 GHz, 4.2 GHz, and 4.3 GHz. At a magnetic field direction of $70°$, caustic angles θ_c are $45°$, $43°$, and $40°$ for the frequencies 4.1 GHz, 4.2 GHz, and 4.3 GHz, respectively. This trend of decreasing θ_c with increasing frequencies is consistent across all magnetic field directions: at $80°$, the θ_c decrease from $45°$ to $39°$, and at $90°$, they decrease from $43°$ to $39°$ as the frequency increases. Note that the uncertainty in defining these angles is approximately $\pm$ $1°$; hence, caustic angles are the same within uncertainty for all ϕ, which is expected for caustics in an external thin-film [18, 19].

3.3.2 Comparative Analysis of Point Source, and Stripline Antenna

The point source simulations show a caustic spin wave beam for all source positions within the microstrip. When the point source is positioned in the middle in Fig. 3.21 (a), it generates a symmetric diamond-shaped pattern with intersection angles defined as $\theta_1 = 95°$, $\theta_2 = 85°$, $\theta_3 = 95°$, and $\theta_4 = 85°$, and the caustics angle is $\theta_c = 43°$ for 4.2 GHz (Table 3.1). Conversely, when the point source is placed at the top shown in Fig. 3.21 (b) and bottom shown in Fig. 3.21 (c), it creates caustics with an intersection angle of $72°$, and the caustics angle of point source is

$\theta_p = 36^\circ$ (not shown in the figure). The energy is focused along specific paths, with the spin waves propagating downward from the top and upward from the bottom.

The spin waves generated by the stripline antenna in Fig. 3.21 (d) exhibit a distinct propagation pattern compared to the point sources. With the static magnetic field oriented at $\phi = 70^\circ$, the stripline antenna generates an initial beam at an angle $\theta_i = 23^\circ$ relative to the x axis, however, from Figs. 3.21 (a), and 3.21 (c), the initial beams are $\theta_i = 27^\circ$, and $\theta_i = 55^\circ$ where initial beam angle 3.21 (a) is almost double of 3.21 (c). The difference between these two angles (ϕ & θ_i) is $\beta = 47^\circ$. Therefore, the caustics angle will be $\theta_c = 43^\circ$, as shown in Table 3.1, which differs from the stripline antenna's $\beta = 47^\circ$. Although the spin wave propagation patterns in Fig. 3.21 show caustic-like beams, these beams are not caustics. However, one important note: a static magnetic field direction $\phi = 70^\circ$, which is approximately equal to the point source direction 72°, shown in Fig. 3.21 (c) with respect to x-axis.

The overlapping image shown in Fig. 3.21 (e) combines the spin wave patterns generated by the point source at the top, bottom, and the stripline antenna. This composite view highlights that the caustics produced by the point sources propagate at different angles as compared to the angles of the beam generated by the stripline antenna. This comparison shows that the mechanism of the beam formation for the microstrip antenna differs from that of the point source excitations.

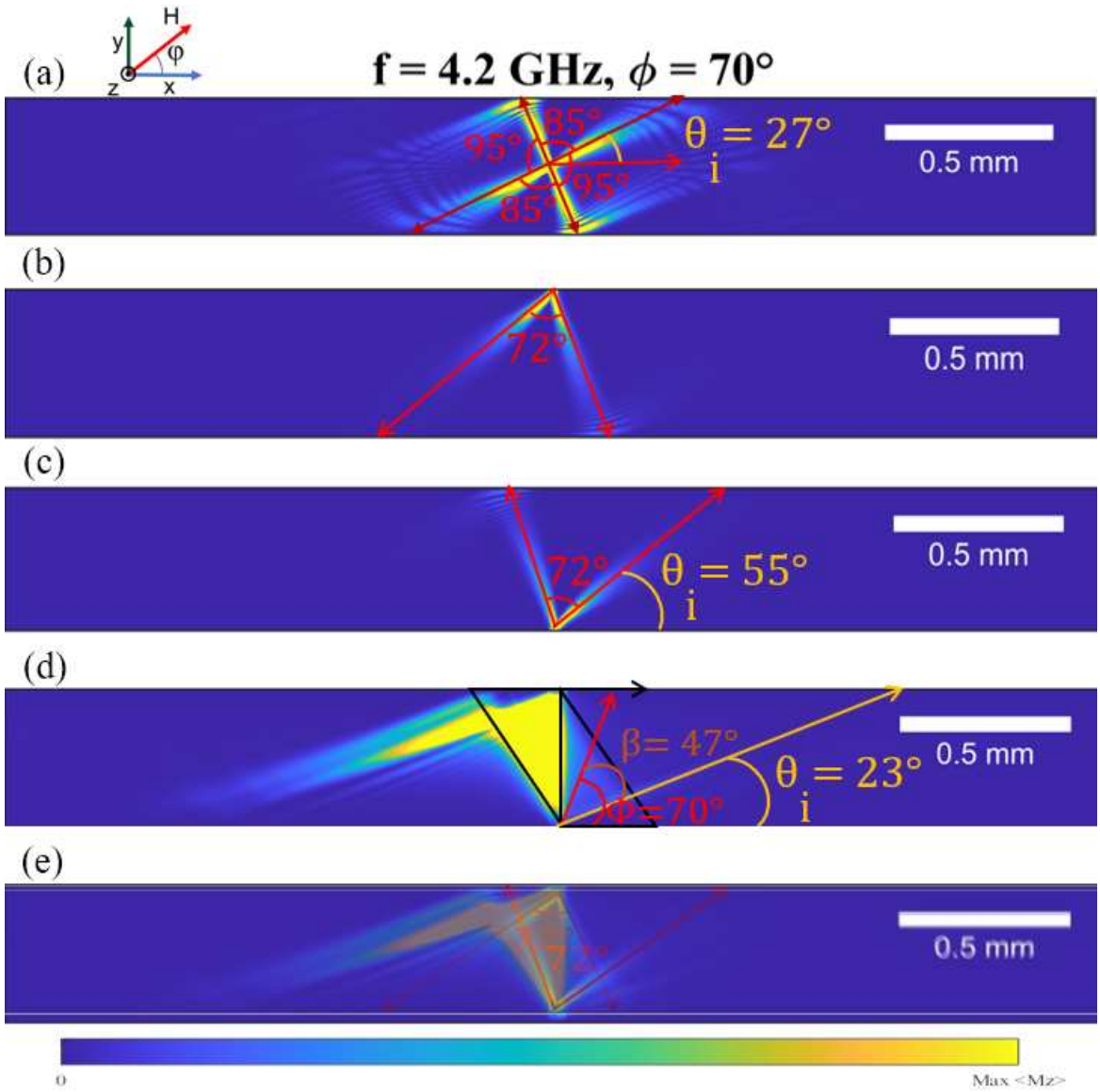

Figure 3.21: Intensity maps from simulations with a damping parameter $\alpha = 0.005$ at a driving frequency of $f = 4.2$ GHz, taken for $\phi = 70°$, and θ_i is the initial beam direction with respect to x axsis. The dimension of microstrip are: length $l = 3276.8$ μm, width $w = 409.6$ μm, and thickness $t = 6$ μm and the static magnetic field $\mathbf{H}$ is 0.0865 T. (a), (b), and (c) show point source configurations with varying intersection angles. (d) displays the spin wave propagation on both sides of the microstrip from the stripline antenna, showing interference patterns where the angle between the static magnetic field $\phi = 70°$and initial beam $\theta_i = 23°$ with respect to x-axis, and $\beta = 47°$. (e) shows overlapping images of spin waves from a point source (point source location at top and bottom) and a stripline antenna.

3.4 Spin Waves Dynamics for a Larger Sample Size

In this section, we used the same sample dimensions as the experimental setup to ensure our simulations closely match the experimental results detailed in Ref. [1]. The microstrip specifications are as follows: length $l = 9011.2$ μm, width $w = 2252.8$ μm, thickness $t = 6.4$ μm, antenna width $w_{\text{antenna}} = 50$ μm, point source diameter $w_{\text{PS}} = 50$ μm, cell size $(1.1 \times 1.1 \times 6.4)$ μm^3, grid size $(8192 \times 2048 \times 1)$, pulse amplitude $\mu_0 h_0 = 0.05$ mT, driving frequency $f = 4.35$ GHz, damping parameter $\alpha = 0.005$, saturation magnetization $M_{\text{s}} = 0.14 \times 10^6$ A/m, exchange stiffness $A_{\text{ex}} = 4.2 \times 10^{-12}$ J/m and static magnetic field applied $\mathbf{H} = 0.0865$ T at angles of $\phi = 70^\circ, 80^\circ$, and 90° with respect to the x-direction.

Figs. 3.22 and 3.23 show snapshots and intensity maps of spin wave propagation simulations at a driving frequency of $f = 4.35$ GHz for point sources (left column) and stripline antennas (right column). The point source generates caustics that lead to half-diamond-shaped patterns that consistently transition from left-tilted to right-tilted shapes across different ϕ angles. The caustic angles for point sources in Fig. 3.23 (left column) exhibit minor variations of a few degrees as the angle ϕ changes from 70° to 80° and 90°. These caustic angles closely match the values listed in Table 3.1, with only slight discrepancies. Conversely, the stripline antenna creates tilted diamond shapes to regular diamond shapes depending on the magnetic field orientation similar to what is observed in the simulations with smaller w, and similar to the experiments. This set of simulations shows that the same principles that apply for the widths of hundreds of microns also apply at the mm length scales used in the experiments [1].

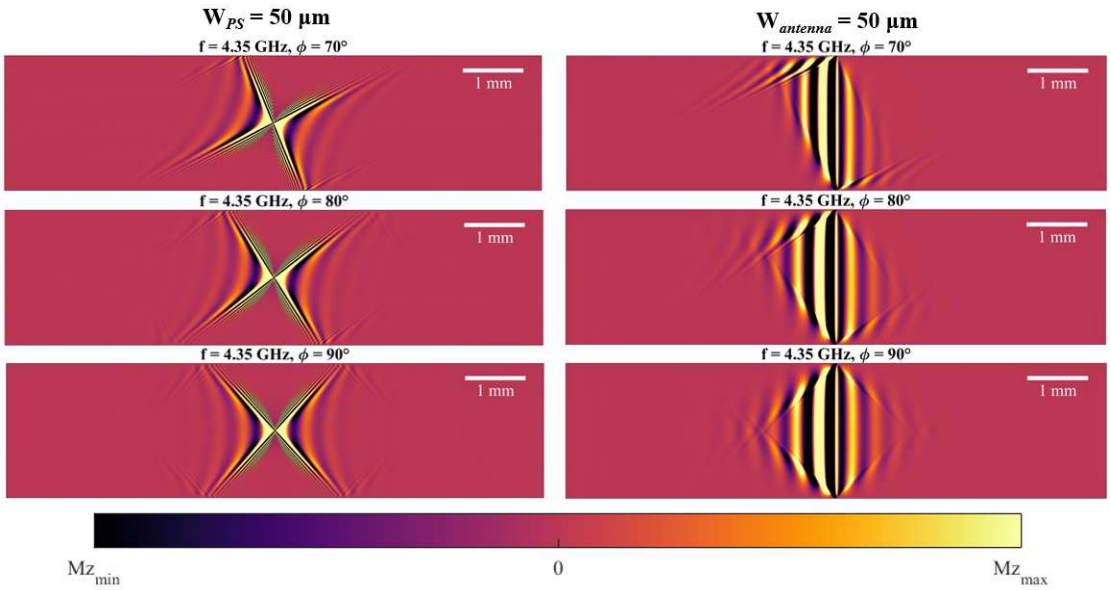

Figure 3.22: Snapshots of spin wave propagation for a width of $w = 2252.8$ μm, antenna width $w_{\text{antenna}} = 50$ μm, point source diameter $w_{\text{PS}} = 50$ μm, damping parameter, $\alpha = 0.005$, driving frequency $f = 4.35$ GHz, are shown for $\phi = 70°$, $80°$, and $90°$. The left column shows point source configurations, while the right column shows stripline antenna configurations.

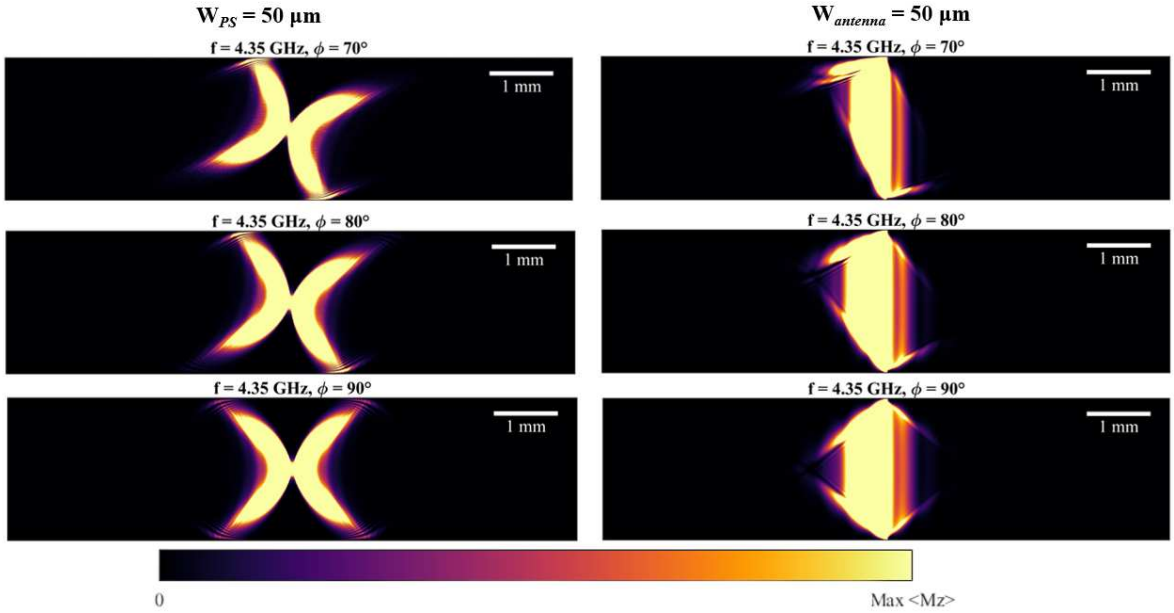

Figure 3.23: Intensity maps of spin wave propagation for a width of $w = 2252.8$ μm, antenna width $w_{\text{antenna}} = 50$ μm, point source diameter $w_{\text{PS}} = 50$ μm, damping parameter, $\alpha = 0.005$, driving frequency $f = 4.35$ GHz, are shown for $\phi = 70°$, $80°$, and $90°$. The left column shows point source configurations, while the right column shows stripline antenna configurations.

Chapter 4

Conclusion

In this thesis, spin wave propagation has been studied in magnetic microstrips made of the Yttrium Iron Garnet (YIG) using micromagnetic simulations. The goal of this research was to investigate spin wave propagation in magnetic microstrips for non-standard magnetic field directions and to understand the formation of spin wave propagation patterns that involve strong, directed initial beams that were observed in recent experiments [1].

Spin wave dispersion relations were calculated by applying a sinc pulse to the middle of a magnetic microstrip using a microstrip antenna and subsequently taking a Fourier transform of the magnetic response. The spin wave dispersion relations show the range of driven frequencies that can excite spin waves. Driven spin wave simulations were also done using a sinusoidal magnetic field. These driven simulations allowed us to obtain the spin wave propagation pattern through the spin propagation snapshots and intensity maps.

The driven simulations were performed at a fixed frequency of $f = 4.2$ GHz, with widths of $w = 0.4096$ mm, 0.2048 mm, and 0.1024 mm, and a range of damping parameters, $\alpha = 0.005$, 0.001, and 0.01. The normalized magnetization m_z component, position in the long axis of the microstrip, and simulation time plot provide detailed information about how spin waves propagate and how they dissipate inside the microstrip. The smaller damping parameter has a larger reflection compared to the large damping parameter. For a microstrip length of $l = 3276.8$ μm, when the damping parameter is $\alpha = 0.001$, the spin wave propagation distance is 3.26 mm with reflection from boundary edges. However, for a larger damping parameter of $\alpha = 0.005$, the propagation distance is reduced to 1.75 mm and it has no reflection at the boundary edges.

For a 90° static magnetic field orientation, the spin waves produced distinct diamond patterns that agree well with experimental observations. As ϕ is reduced from 90° to 80°, and then to 70°, the diamond patterns become tilted diamonds with progressively larger tilt angles. The spin wave caustics are highly directional and the directions depend on the driving frequency and the

static magnetic field directions. Additional simulations were done using a point source to create spin wave caustics in order to compare the diamond patterns to the shapes that are generated by caustics. The interference patterns of width-quantized modes, and the caustic angles and diamond outline are not an exact match for $\phi = 80^\circ$ and 70°, we expect that the tilted diamond patterns also involved width-quantized modes, though the explanation is likely more involved than for $\phi = 90^\circ$ degrees due to the broken symmetry.

The width quantization is one of the crucial factors that can be explained with the help of an isofrequency curve [11, 15]. Width quantization occurs when the wavevector is quantized in confined geometries. For large widths, many modes can be excited, which can lead to complex spin wave propagation patterns. Reducing the width w from 0.4096 mm, 0.2048 mm, and 0.1024 mm, leads to progressively larger mode spacing and consequently progressively fewer modes are excited. For the smallest width, only a single mode is excited and the propagation pattern resembles a snake tail for $\phi = 70^\circ$, and 80° degrees.

The point source simulations were conducted by positioning the point source at three locations: the top, middle, and bottom of the microstrip. These point source simulations were compared with the stripline antenna. The point source creates spin wave caustics, and the stripline antenna forms the initial beams. These initial beams were observed in experiments as a bright beam coming from the bottom left of the microstrip at a short distance from the microstrip antenna [1]. The point source's caustic beams produce a diamond outline that matches with spin-wave caustic angles but it does not match the angle of the tilted diamond outline. The beam observed in the experiment, generated from the microstrip antenna, is part of the tilted diamond pattern and is likely produced by width-quantized modes, and it also depends on static magnetic field directions ϕ and the microstrip's structure.

Finally, we performed simulations for dimensions that matched the experimental results and showed that the observations at smaller length scales also apply to samples with millimeter dimensions. These results are important for the development of magnonics devices that use patterned defects inside the microstrip to control spin waves and pave the way for innovations in information

processing technologies. The next step in this work is to develop a theoretical model to explain the spin wave propagation patterns.

Bibliography

[1] Mitchell S. Swyt, Lia Compton, Arturo Reyes-Almanza, César L. Ordóñez Romero, Giuseppe Pirruccio, H. J. Liu, and Kristen S. Buchanan. Magnonic notch filter based on spin wave caustic beams. *Applied Physics Letters*, 124(11), 2024.

[2] Atsufumi Hirohata, Keisuke Yamada, Yoshinobu Nakatani, Ioan-Lucian Prejbeanu, Bernard Diény, Philipp Pirro, and Burkard Hillebrands. Review on spintronics: Principles and device applications. *Journal of Magnetism and Magnetic Materials*, 509:166711, 2020.

[3] Abdulqader Mahmoud, Florin Ciubotaru, Frederic Vanderveken, Andrii V. Chumak, Said Hamdioui, Christoph Adelmann, and Sorin Cotofana. Introduction to spin wave computing. *Journal of Applied Physics*, 128(16), 2020.

[4] Anjan Barman, Gianluca Gubbiotti, Sam Ladak, Adekunle Olusola Adeyeye, Maciej Krawczyk, Joachim Gräfe, Christoph Adelmann, Sorin Cotofana, Azad Naeemi, Vitaliy I Vasyuchka, et al. The 2021 magnonics roadmap. *Journal of Physics: Condensed Matter*, 33(41):413001, 2021.

[5] Anil Prabhakar and Daniel D. Stancil. *Spin Waves: Theory and Applications*, volume 5. Springer, 2009.

[6] A. A. Serga, A. V. Chumak, and Burkard Hillebrands. YIG magnonics. *Journal of Physics D: Applied Physics*, 43(26):264002, 2010.

[7] Alexander Khitun and Kang L. Wang. Nano scale computational architectures with spin wave bus. *Superlattices and Microstructures*, 38(3):184–200, 2005.

[8] M. P. Kostylev, A. A. Serga, T. Schneider, B. Leven, and B. Hillebrands. Spin-wave logical gates. *Applied Physics Letters*, 87(15), 2005.

[9] Andrii V. Chumak, Alexander A. Serga, and Burkard Hillebrands. Magnon transistor for all-magnon data processing. *Nature communications*, 5(1):4700, 2014.

[10] Frank Heussner, Matthias Nabinger, Tobias Fischer, Thomas Brächer, Alexander A. Serga, Burkard Hillebrands, and Philipp Pirro. Frequency-division multiplexing in magnonic logic networks based on caustic-like spin-wave beams. *Physica Status Solidi (RRL)–Rapid Research Letters*, 12(12):1800409, 2018.

[11] Matthew G. Copus, Alexandra R. Stuart, Robert E. Camley, and Kristen S. Buchanan. Spin wave dispersion relations and isofrequency curve calculations using micromagnetic simulations. *Journal of Applied Physics*, 132(12), 2022.

[12] Arne Vansteenkiste, Jonathan Leliaert, Mykola Dvornik, Mathias Helsen, Felipe Garcia-Sanchez, and Bartel Van Waeyenberge. The design and verification of mumax3. *AIP Advances*, 4(10), 2014.

[13] Jonas J. Joos, Pedram Bassirian, Pieter Gypens, Jeroen Mulkers, Kai Litzius, Bartel Van Waeyenberge, and Jonathan Leliaert. Tutorial: Simulating modern magnetic material systems in mumax3. *Journal of Applied Physics*, 134(17), 2023.

[14] Sebastian Neusser and Dirk Grundler. Magnonics: Spin waves on the nanoscale. *Advanced Materials*, 21(28):2927–2932, 2009.

[15] Zhizhi Zhang, Michael Vogel, José Holanda, Junjia Ding, M Benjamin Jungfleisch, Yi Li, John E. Pearson, Ralu Divan, Wei Zhang, Axel Hoffmann, et al. Controlled interconversion of quantized spin wave modes via local magnetic fields. *Physical Review B*, 100(1):014429, 2019.

[16] A. V. Chumak, A. A. Serga, S. Wolff, B. Hillebrands, and M. P. Kostylev. Scattering of surface and volume spin waves in a magnonic crystal. *Applied Physics Letters*, 94(17), 2009.

[17] V. Veerakumar and R. E. Camley. Magnon focusing in thin ferromagnetic films. *Physical Review B*, 74(21):214401, 2006.

[18] Alexis Wartelle, Franz Vilsmeier, Takuya Taniguchi, and Christian H. Back. Caustic spin wave beams in soft thin films: Properties and classification. *Physical Review B*, 107(14):144431, 2023.

[19] T. Schneider, A. A. Serga, A. V. Chumak, C. W. Sandweg, S. Trudel, S. Wolff, M. P. Kostylev, V. S. Tiberkevich, A. N. Slavin, and B. Hillebrands. Nondiffractive subwavelength wave beams in a medium with externally controlled anisotropy. *Physical Review Letters*, 104(19):197203, 2010.

[20] Frank Heussner, Giacomo Talmelli, Moritz Geilen, Björn Heinz, Thomas Brächer, Thomas Meyer, Florin Ciubotaru, Christoph Adelmann, Kei Yamamoto, Alexander A. Serga, et al. Experimental realization of a passive gigahertz frequency-division demultiplexer for magnonic logic networks. *Physica Status Solidi (RRL)–Rapid Research Letters*, 14(4):1900695, 2020.

[21] V. V. Kruglyak, S. O. Demokritov, and D. Grundler. Magnonics. *Journal of Physics D: Applied Physics*, 43(26):264001, 2010.

[22] Johannes Stigloher, Martin Decker, Helmut S. Körner, Kenji Tanabe, Takahiro Moriyama, Takuya Taniguchi, Hiroshi Hata, Marco Madami, Gianluca Gubbiotti, Kensuke Kobayashi, et al. Snell's law for spin waves. *Physical Review Letters*, 117(3):037204, 2016.

[23] Sang-Koog Kim, Sangkook Choi, Ki-Suk Lee, Dong-Soo Han, Dae-Eun Jung, and Youn-Seok Choi. Negative refraction of dipole-exchange spin waves through a magnetic twin interface in restricted geometry. *Applied Physics Letters*, 92(21), 2008.

[24] R. G. Kryshtal and A. V. Medved. Influence of magnetic anisotropy on dynamic magnonic crystals created by surface acoustic waves in yttrium iron garnet films. *Journal of Magnetism and Magnetic Materials*, 426:666–669, 2017.

[25] V. N. Krivoruchko and A. S. Savchenko. Controlled refraction and focusing of spin waves determined by the aharonov-casher effect. *Physical Review B*, 109(18):184437, 2024.

[26] Philipp Pirro, Thomas Brächer, Katrin Vogt, Björn Obry, Helmut Schultheiss, Britta Leven, and Burkard Hillebrands. Interference of coherent spin waves in micron-sized ferromagnetic waveguides. *Physica Status Solidi (b)*, 248(10):2404–2408, 2011.

[27] Sankha Subhra Mukherjee, Jae Hyun Kwon, Mahdi Jamali, Masamitsu Hayashi, and Hyunsoo Yang. Interference-mediated modulation of spin waves. *Physical Review B*, 85(22):224408, 2012.

[28] Mateusz Gołębiewski, Paweł Gruszecki, Maciej Krawczyk, and Andriy E. Serebryannikov. Spin-wave talbot effect in a thin ferromagnetic film. *Physical Review B*, 102(13):134402, 2020.

[29] Mohammad Haidar. Interference patterns of propagating spin wave in spin-hall oscillator arrays. *Journal of Applied Physics*, 135(22), 2024.

[30] Eugene Hecht. *Optics, 5e*. Pearson Education India, 2002.

[31] Yu Hao, R. E. Camley, and Z. Celinski. Influence of magnetic external field and particle size on the formation of a single domain state. *Journal of Magnetism and Magnetic Materials*, 589:171523, 2024.

[32] Lin Sun, Lei Guo, Guocai Wang, Hua Su, Bo Liu, and Xiaoli Tang. A high-speed and power-efficient gradient-pulse injection method for spin-transfer torque magnetic random-access memory. *Applied Physics Letters*, 123(3), 2023.

[33] M. T. Islam, M. A. J. Pikul, and X. S. Wang. Thermally assisted magnetization reversal of a magnetic nanoparticle driven by a down-chirp microwave field pulse. *Journal of Magnetism and Magnetic Materials*, 537:168174, 2021.

[34] Jonas De Clercq, Arne Vansteenkiste, Medjid Abes, Kristiaan Temst, and Bartel Van Waeyenberge. Modelling exchange bias with mumax3. *Journal of Physics D: Applied Physics*, 49(43):435001, 2016.

[35] M. T. Islam, M. A. S. Akanda, F. Yesmin, M. A. J. Pikul, and J. M. T. Islam. Role of shape anisotropy on thermal gradient-driven domain wall dynamics in magnetic nanowires. *Modern Physics Letters B*, 37(12):2350013, 2023.

[36] M. Donahue. The object oriented micromagnetic framework (OOMMF) project at itl/nist. *http://math. nist. gov/oommf*, 1998.

[37] Marijan Beg, Martin Lang, and Hans Fangohr. Ubermag: Toward more effective micromagnetic workflows. *IEEE Transactions on Magnetics*, 58(2):1–5, 2021.

[38] Jiabin Zhang, Weichao Yu, Xiheng Chen, and Jiang Xiao. A frequency-domain micromagnetic simulation module based on comsol multiphysics. *AIP Advances*, 13(5), 2023.

[39] Arne Vansteenkiste and Ben Van de Wiele. Mumax: A new high-performance micromagnetic simulation tool. *Journal of Magnetism and Magnetic Materials*, 323(21):2585–2591, 2011.

[40] Thomas L. Gilbert. A phenomenological theory of damping in ferromagnetic materials. *IEEE Transactions on Magnetics*, 40(6):3443–3449, 2004.

[41] Amikam Aharoni. *Introduction to the Theory of Ferromagnetism*, volume 109. Clarendon Press, 2000.

[42] William Fuller Brown Jr. Thermal fluctuations of a single-domain particle. *Physical Review*, 130(5):1677, 1963.

[43] Vladislav E. Demidov, Johann Jersch, Sergej O. Demokritov, Karsten Rott, Patryk Krzysteczko, and Guenter Reiss. Transformation of propagating spin-wave modes in microscopic waveguides with variable width. *Physical Review B*, 79(5):054417, 2009.

[44] M. C. Onbasli, Andreas Kehlberger, Dong Hun Kim, Gerhard Jakob, Mathias Kläui, Andrii V. Chumak, Burkard Hillebrands, and Corey Alexander Ross. Pulsed laser deposition of epitaxial yttrium iron garnet films with low gilbert damping and bulk-like magnetization. *APL Materials*, 2(10), 2014.

[45] Natalie Whitehead. *Making the Grade: Generating & Controlling Spin Waves with a Graded Refractive Index*. University of Exeter (United Kingdom), 2019.